Multidimensional Tomographic Imaging Using Volume Holography

GEORGE BARBASTATHIS, MEMBER, IEEE, AND DAVID J. BRADY, MEMBER, IEEE

Invited Paper

We propose the application of volume holography to four-dimensional (4-D) spatiospectral imaging. The proposed systems use materials and techniques developed for holographic data storage and interconnections to capture three-dimensional (3-D) spatial and one-dimensional (1-D) spectral information about a remote light source or scatterer. We analyze case studies of simple architectures using spherical-reference volume holograms as imaging elements in a fluorescence confocal microscope arrangement and demonstrate the equivalence of the holographic degeneracies with a slicing operation on the reconstructing incoherent source. We develop a general theoretical framework for the diffraction of random fields from volume holograms and show that the formulation can be used as an imaging design tool. Applications and future directions are also discussed.

***Keywords*—** *Holography, microscopy, optical imaging, tomography.*

I. INTRODUCTION

The introduction of volume holography in a seminal paper by van Heerden [1] was soon followed by the discovery of appropriate materials through the effect of "optical damage" [2], which later became known as the photorefractive effect [3]. Since then, volume holograms have been popular in a number of subareas of optical information processing, namely data storage [1], [4]–[6], interconnects and artificial neural networks [7], [8], and communications [9]–[13]. To date, commercial applications of thick volume holograms are for spectral filtering [14] and three-dimensional (3-D) storage devices. In this paper we introduce a novel application of volume holography to multidimensional imaging.

Manuscript received November 19, 1998; revised April 23, 1999. This work was supported by the Defense Advanced Research Projects Agency.

G. Barbastathis was with the Beckman Institute for Advanced Science and Technology, University of Illinois at Urbana-Champaign, Urbana-Champaign, IL 61801 USA. He is now with the Department of Mechanical Engineering, Massachusetts Institute of Technology, Cambridge, MA 02139 USA.

D. J. Brady is with the Beckman Institute for Advanced Science and Technology and the Department of Electrical and Computer Engineering, University of Illinois at Urbana-Champaign, Urbana, IL 61801 USA.

Publisher Item Identifier S 0018-9219(99)09560-2.

Optical imaging is in the midst of a revolutionary shift from analog to digital systems. The most apparent aspects of this shift are the ubiquitous availability of digitized images and the use of digital networks to transmit images. Deeper aspects of the shift to digital techniques are only beginning to be explored, however. For example, the physical analogy between the detected field and the perceived object which is the basis of classical imaging need not be present in a digital system. In classical systems, a two-dimensional (2-D) focal plane pattern is used to represent the object in spite of the fact that the object is usually 3D. The goal in building a classical system is to make the field distribution on the sensor plane appear as similar as possible to the object viewed from the same perspective. Digital systems, in contrast, use sensor data to reconstruct the object in its native 3-D space. Since the digital system does not directly display sensor data, sensor data need not look like the object. The goal in designing a digital system is to maximize the detected object information so as to allow an accurate object model to be constructed. In many cases, it may not be possible to obtain simultaneously information on all object features. For example, capture of polarization data may preclude capture of spectral data or reduce spatial resolution, capture of temporal variations may limit 3-D resolution, etc. In view of these tradeoffs, digital systems are designed to optimize the capture of specific features of interest.

Imaging system design has been the primary subject of physical optics for millenia and the state of development of these systems is very high. While volume holograms can replicate the function of imaging system components, such as lenses, beam splitters, and spatial or spectral filters, holograms do not out perform conventional components for these functions. Volume holography as a tool is extremely attractive in emerging digital imaging systems, however, because volume holograms have more design degrees of freedom per unit system aperture than any other optical component. Design complexity allows volume holograms to extract more sophisticated features from fields, enabling sensor design to target features for object reconstruction.

Volume holograms for complex field transformation and feature extraction have been highly developed in the context of holographic storage and interconnection. Digital data storage, where each stored hologram corresponds to a page of information, is the most straighforward application. Despite this apparent simplicity, system geometry is extremely important to the capacity and function of data storage. On the next level of complexity, artificial neural networks have used holographic mappings for dendritic interconnections. Before the spectacular improvement of very large scale integration (VLSI) technology in the 1990's [15], [16], volume holograms were considered as a primary contender for the efficient storage and implementation of the massive interconnections needed for complex pattern recognition tasks. Many of the design considerations from data storage and neural net systems can be applied to the design of holograms for imaging applications. As will become evident in the remainder of the paper, some of the fundamental properties of holographic storage techniques, in particular the spatial selectivity and degeneracies of spherical reference volume holograms [17], can be applied verbatim to imaging. Even though the architectures we study here are different than the disk geometry of [17], the similarity simplifies our intuitive understanding of the problem.

The structure of the paper is as follows. Section II provides an extensive introduction to holographic storage and some of the issues arising when building a volume holographic system. In Section III we touch upon the primary issues arising in computational imaging systems and show as a simple example that the performance of the common fluorescence microscope arrangement improves when the collector lens is replaced by a volume hologram. In Section IV we analyze three simple implementations of a particular transformation, a matched filter to a point source, using volume holograms. We show that, when viewed on a flat camera detector, the diffracted field reconstructs a color-variant slice of the originating incoherent source, and we derive the slice shape as a function of the recording and reconstructing geometries. In Section V we develop a general procedure, formally equivalent to the Hopkins integral, for the calculation of diffraction of random optical fields from volume holograms. Our formulation leads to a design process, based on coherent mode decomposition, for constructing a volume hologram capable of shaping the coherence properties of the optical field arbitrarily, within the allowable degrees of freedom. We conclude in Section VI by discussing design considerations for multidimensional imaging systems, their markets, and applications.

II. Holographic Storage

Holographic storage is motivated by high overall data capacity and parallel access. It was introduced by van Heerden [1], who first noted the similarity between X-ray diffraction from periodic crystal lattices and light diffraction from volume gratings and proposed utilizing this effect to superimpose and selectively retrieve multiple holograms in the same material volume, each hologram storing one page of information. The maximum number of resolvable voxels that can be stored inside a volume V at wavelength λ is V/λ^3. This corresponds to an order of 10 Tbits/cm^3 for green light. The parallelism, or the maximum number of resolvable pixels that can fit in a single page (i.e., an individual hologram), is bounded above roughly by $V^{2/3}/\lambda^2$. For green light, this is 0.4 Gbits/cm^2, with a data rate of several Gbits/s if the page size is actually 1 cm $\times$ 1 cm, and it takes no more than a few milliseconds to integrate each individual hologram on the detector. Neither of these upper bounds has ever been achieved in practice because of material and device limitations.

A typical holographic storage system is shown in Fig. 1. The hologram is recorded by illuminating a photosensitive material with the interference pattern formed by two coherent light beams, the reference and signal. The signal beam contains the information to be stored in the form of transverse phase or amplitude modulation of the beam profile, imposed by a spatial light modulator (SLM). The reference beam contains no information, except the "identity" of the hologram. For example, in the most common form of holographic storage, called "angle-multiplexing" [18]–[20], which is depicted in Fig. 1, the reference beam for the mth hologram is a plane wave incident at angle θ_m. After the exposure is complete, each hologram ideally contributes an equal amount of spatial modulation to the refractive index of the material. The mth hologram is then accessed selectively by illuminating the exposed material with the corresponding plane wave at angle θ_m. If the original recording reference beams were appropriately spaced, then the diffracted light contains significant reconstruction from the mth hologram only. The remaining holograms are Bragg mismatched, i.e., they are read out by the incident beam, but their reconstructions, when integrated over the entire volume of the material, cancel out to zero. In the common configuration of Fig. 1, the angular separation between adjacent holograms must be equal, approximately, to an integral multiple of

$$\Delta\theta = \frac{\lambda}{2L\sin\theta}. \tag{1}$$

This quantity is known as angle Bragg selectivity. Since $\Delta\theta$ is proportional to λ/L, the selectivity improves by using shorter wavelengths or thicker materials. It is important to note that the multiplexed holograms share the entire volume of the recording material; therefore, holographic storage is fundamentally different than layered volume storage methods, such as the digital video disk (DVD) and two-photon storage [21]. One might think of the process of Bragg matching a single hologram in the presence of multiple holograms sharing the medium as similar to tuning a receiver to a radio station; the matching angle θ_m corresponds to the resonance frequency of the receiver, and the Bragg separation $\Delta\theta$ corresponds to the quality factor Q that determines the receiver bandwidth.

Angle multiplexing has been by far the most popular technique in experimental demonstrations. The angular

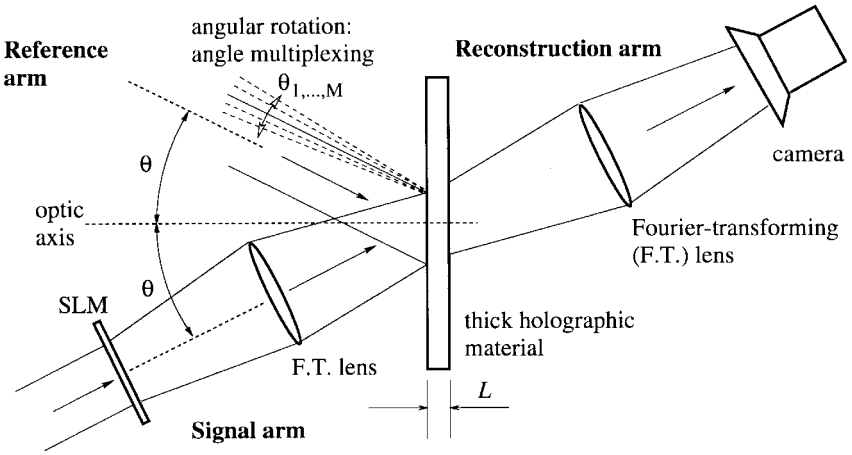

Fig. 1. A common holographic memory architecture. The mth hologram is recorded by the interference of the beams from the "reference" (incident at θ_m) and "signal" arms (incident at angle θ). The information to be stored is modulated on the signal wavefront by the SLM. When the hologram is illuminated by a plane wave incident at angle θ_m from the reference arm, the mth stored page is diffracted into the "reconstruction" arm and is focused onto the camera. This scheme is called "angle multiplexing."

deflection required to record and access different holograms has been implemented by electromechanical actuation of off-the-shelf commercial mirrors [5], [6], [22]–[24], magnetic actuation of micromachined mirror flaps [25], acoustooptic deflection [26], [27], and liquid-crystal-based electrooptic deflection [28], [29].

Alternative multiplexing methods have also been devised. For example, using a plane wave reference beam, the reconstruction is also sensitive to the wavelength of the incident beam [18], [19], [30], [31]. With widely tunable visible and near-IR lasers becoming more common, compact, long lived, and affordable, the elimination of the need for an angular deflector makes wavelength multiplexing a more attractive choice. Another method without mechanical addressing requirement is phase-code multiplexing [32] where the reference beams are implemented as a set of orthogonal codes and addressed using a phase SLM. Even simpler is the implementation of shift multiplexing, which requires a reference beam that is either a collection of plane waves with a regular relative angle displacement [33] or which is a spherical wave [17]. In both cases, individual holograms are accessed by relative translation between the reference and the recording medium. The required shift between adjacent holograms is typically of the order of a few micrometers. The shift could be implemented acoustooptically, but mechanical translation is simpler and well characterized because of the popularity of optical storage disks [34]. Therefore, the latter has been the method of choice in high-capacity experiments [35], [36]. The properties of spherical reference volume holograms will be revisited in detail in Section IV.

The techniques mentioned so far make use of Bragg mismatch to multiplex holograms. Further increase in capacity may be obtained by synthetically increasing the aperture of the hologram using the motion of the reference beam. In the holographic storage jargon, these techniques are referred to as "fractal" [37]. Recent implementations include the "peristrophic" multiplexing method [38] and the hybrid angle-wavelength multiplexing method [39]. The aperture increase is effected by use of the degeneracy effects that will be derived for some specific geometries, but in quite a different context, in Section IV-C.

With a wide choice of well-understood multiplexing techniques available, the next critical system issue is the material [40], which is determined by the application. We consider photorefractive and photopolymer materials only, because so far they have been the most popular in experiments of erasable and permanent holographic storage, respectively. A complete review of available holographic storage materials [41] is outside the scope of this paper.

Photorefractive crystals, such as Fe-doped $LiNbO_3$, $Sr_xBa_{1-x}NbO_3$ (SBN:x), and $BaTiO_3$ were the first materials to be used for holographic storage [3]. During recording, the refractive index change occurs via the electrooptic effect after a spatially varying space-charge field is established in the crystal from the diffusion or drift of photo-excited charges away from the illuminated regions [42]–[44]. The space-charge field sustains itself after removal of the recording beams but decays because of thermal electronic excitation in the dark, or uniform photo-excitation during hologram readout. Decay occurs also as a result of superimposing more holograms in the same location of the material. As a result of the erasure of existing holograms when new holograms are recorded, the dynamic range of the material is not fully utilized, and the diffraction efficiency (defined as the portion of the reference beam power diffracted into the hologram) of $M \gg 1$ equal-strength holograms is [45], [46]

$$\eta(M) = \frac{(M/\#)^2}{M^2}. \tag{2}$$

The parameter $M/\#$ (pronounced "M-number") depends highly on material parameters, such as absorption coefficient, doping levels, recombination lifetimes, etc., but

also on the beam profiles and intensities and stability of the experimental arrangement; it is, therefore, a system parameter [46]. Typical photorefractives have $M/1$ or less, but there are exceptions [22].

Photorefractive holograms are semipermanent, and, therefore, appropriate for optically erasable, rewritable, and refreshable random access memory architectures [5], [22]–[24], [29], [47], or when dynamic holography is required, e.g., two-wave mixing [48], [49], phase conjugation [50], [51], optical novelty filters [52], self-waveguiding [53], [54], etc. Photorefractives are often used also in applications that require permanent storage, because the crystal thickness can be large (several millimeters or centimeters), thus providing high capacity. A number of techniques exist for recording permanent holograms in photorefractives and include thermal fixing [55]–[60], electrical fixing [61]–[65], two-lambda readout [66]–[70], and two-photon recording [71]–[75]. A comprehensive review of nonvolatile photorefractive storage is given in [76].

A different class of holographic recording mechanisms is based on photochemical changes initiated by exposure to the recording beams. The most common example is photoinduced polymerization in the DuPont polymer HRF-150 [77]–[79], where recording occurs as refractive index modulation because of density changes in the exposed areas; it is permanent and does not significantly degrade over time. Despite the different recording mechanism, the diffraction efficiency as a function of number of superimposed holograms still follows the rule (2). The HRF-150 has been demonstrated to have approximately $M/6$, and has been used successfully in a number of high-capacity demonstrations of holographic storage [35], [80], [81].

The selection of material and multiplexing technique depends on the application. Storage in photopolymers is permanent, hence they target read-only (ROM) or write-once-read-many (WORM) storage applications. Unfortunately, the thickness of photopolymer films is limited by considerations of mechanical stability and optical quality. The highest capacity ever achieved in the DuPont polymer is 12 bits/μm^2 [35] using shift multiplexing with a 100 μm thick film. This surface density is higher than the DVD-ROM by a factor of two. Recently, samples of thickness up to 5 mm were fabricated using a poly(methyl-methacrylate) (PMMA) polymer matrix to host the photosensitive material phenanthrenequinone (PQ) [82]–[84]. Theoretical calculations [17], [85] show that the achievable density at 5 mm hologram thickness is as high as 200 bits/μm^2. Therefore, PQ-doped PMMA seems promising as a replacement to the DuPont HRF-150 polymer and nonvolatile photorefractive storage for permanent high-density holographic memories.

Other systems issues that are important for holographic storage are page-oriented error correction [86]–[88] and channel modulation [89], [90], pixel matching [91] (i.e., minimizing aberration distortion by using unit magnification in the optical system between the SLM and the detector), and the location of the hologram with respect to the imaging system [92] (i.e., whether the hologram should be located on the focal or pupil plane of the imaging system that maps the SLM on the detector plane). A complete review of these issues is outside the scope of the present paper.

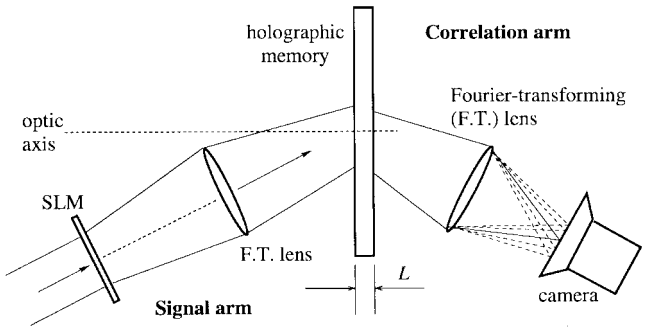

Fig. 2. Operation of the angle-multiplexed holographic memory of Fig. 1 in correlator mode.

The function of volume holograms as correlators [93] has been traditionally an important application of holographic memories oriented toward optical pattern recognition [94]–[96]. Suppose M patterns f_m $(m = 1, \ldots, M)$ are stored in a holographic memory. If the memory is illuminated by a new pattern g along the path of the signal beam, and a Fourier-transforming lens is placed on the continuation reference path (see Fig. 2), then at the focal plane one obtains the correlations $g \star f_m$ of the novel pattern with all the stored patterns at once. The parallel correlation operation is obtained at the expense of losing shift invariance in one dimension at the output plane. This mode of operation of a holographic memory has been successfully used in a number of applications [97]–[99]. In Sections IV and V we will show that the volume hologram correlates its internal modes with the input field. This function is useful as an imaging operation.

III. 3-D Imaging and Volume Holography

A. Types of Imaging Systems

An optical imaging system transfers information about an object to the user, using light as information carrier. The amount and quality of the transmitted information is determined by the propagation properties of light. Free space propagation has the effect of delocalizing the object features, "blurring" the image. Optical elements, such as lenses, are used to compensate propagation and recover the object features locally or bring the image "in focus."

Most imaging instruments assume planar objects, i.e., objects that can be described by a two-variable function defined on a surface transverse to the optical axis (see Fig. 3). The optical system performs an analog linear transformation on the transverse field intensity distribution, and the image appears at the final detection stage. The imaging task is more demanding for 3-D objects, because it requires compensation of light propagation effects in three dimensions. Unfortunately optical instruments are geared to handle planar rather than volumetric objects, and optical detectors are also typically planar (2D). Three-

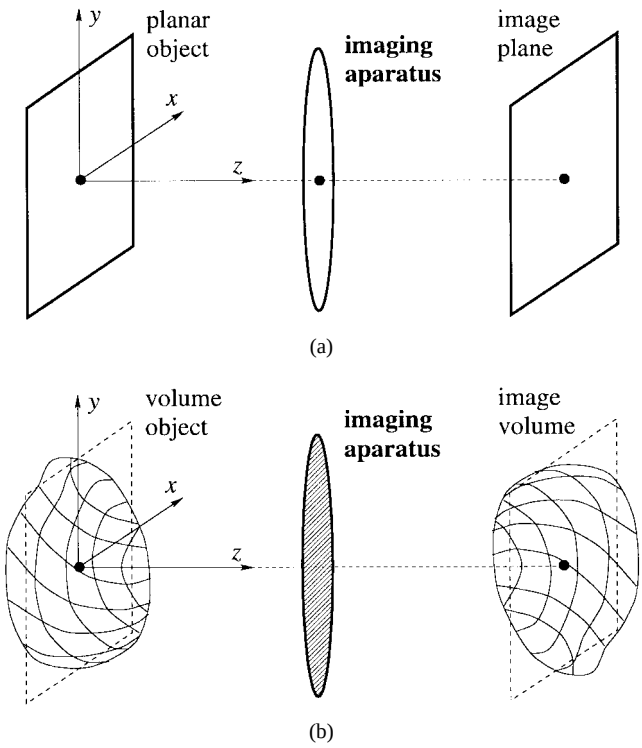

Fig. 3. (a) A planar imaging geometry. (b) A volume imaging geometry. The dashed lens indicates that the imaging system is usually more complicated than a single lens.

dimensional imaging requires the acquisition of sets of lower-dimensional intensity measurements (2-D or point measurements) and the subsequent formation of the image from these measurements. One selection for the intermediate measurements may be 2-D images of slices of the 3-D object. The imaging system is then called "tomographic." The content of the intermediate measurements, however, may not resemble the object at all. Then, a more complicated transformation is required to recover the image. This class of "computational imaging" systems is quickly becoming more popular as the available digital processing power increases.

Three-dimensional optical imaging schemes may be classified into five broad categories: scanned systems; scene analysis systems; projective systems; interferometric systems; and modal systems. Scanned systems include laser spot scanners, confocal microscopes, and laser fluorescence microscopes. These systems are effective but slow, since the volume data are acquired one spot at a time. Scene analysis systems combine expert systems and geometry to computationally reconstruct objects; they require substantial prior object knowledge. Projective systems combine ray optics and inverse-Radon or similar transforms to reconstruct objects and work best with high depth of field optical components. Interferometric systems include holographic schemes and coherence tomography; they are very powerful and general but are subject to noise concerns. Modal systems take the most general approach, detecting the state of all optical modes and attempting a computational inversion. All five imaging system classes require new approaches to

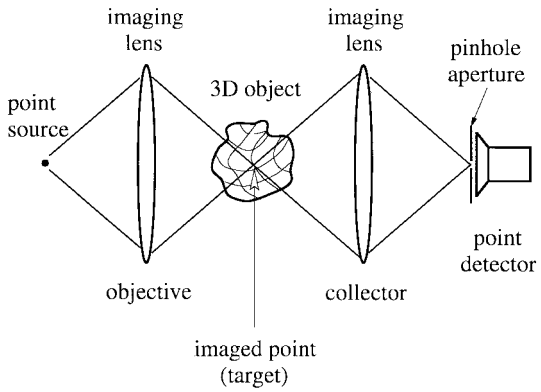

Fig. 4. Principle of the confocal microscope arrangement. In experimental configurations, the sample is sometimes: 1) reflective, when the system is folded, sharing the same lens as objective and collector, or 2) fluorescent, when the radiation emitted by the sample is at a longer wavelength and the illuminating radiation is blocked by a color filter.

optical design and benefit from spatial and spectral filtering. Volume holographic elements can substantially improve any type of imaging system. In this paper we will illustrate this potential for the cases of confocal microscopy, tomography, and coherence imaging. The following paragraphs describe the traditional approaches to confocal microscopy and coherence imaging in more detail.

The confocal microscope, invented by Minsky [100], operates by the lowest dimensional measurements possible, i.e., point measurements. A confocal microscope is sketched schematically in Fig. 4. It constructs a 3-D image by scanning the volume of the specimen and obtaining the emitted intensity values one point at a time. The geometry of the optical system is such that light emitted locally from a very small portion of the object only is allowed to reach the detector. The rest of the light is rejected by the aperture at the detector pupil. The proportional light contribution to a single measurement as function of object coordinates is equivalent to the 3-D point-spread function (PSF) of the system; it can be calculated accurately under various aberration conditions using Fourier optics [101], [102]. Confocal microscopy has been implemented in many different variants for improved light efficiency or resolution, e.g., differential interference [103], fluorescence [104], two-photon [105], etc.; it has been spectacularly successful, primarily in various applications of biological and biomedical imaging.

Coherence imaging (Fig. 5) is an example of computational imaging that relies on global, rather than local, measurements. It is based on a fundamental result, derived independently by van Cittert and Zernicke [106], [107], which states that the degree of statistical correlation of the optical field in the far zone, expressed as a complex function over the exit pupil of the imaging system, is the Fourier transform of the object intensity distribution. Therefore, the object can be recovered by measuring the coherence function through interferometry and then inverse-Fourier transforming the result. The application of the van Cittert–Zernicke theorem in the radio frequency spectral

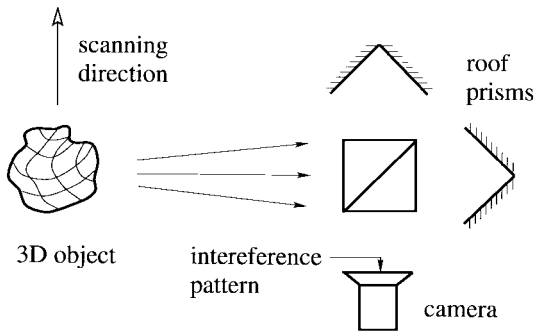

Fig. 5. A system for implementing coherence imaging with a "rotational shear interferometer" (after [116]). The roof prisms rotate the image antisymmetrically about the two axes, and the two versions are interfered at the camera plane.

region is the basis of radio astronomy [108], which yields by far the most accurate images of the most remote cosmic objects. The most common formulation of the theorem relates the mutual coherence in a plane at infinity to a 2-D source intensity distribution, but extentions to 3-D sources have been derived by various authors [109]–[112]. The far-field version of the extended van Cittert–Zernicke theorem was recently implemented experimentally [113]–[115]. A full generalization of the theorem has also been developed and experimentally implemented to allow Fresnel zone reconstruction in projective coordinates [116].

In either of these systems the detected intensity is shaped by the response of the imaging elements (in the confocal microscope, the intensity measurement results from the field received at a single point, whereas in coherence imaging the measured intensity is the result of interference between two or more optical paths). A volume hologram is a more general design tool. One may think of it as an element that modifies an optical beam continuously along an entire volume. As such, it can be designed to perform spatial filtering operations similar to the confocal microscope, but it is more sophisticated because of the additional third degree of freedom, as we show in an example in Section III-C. An even more extended operation available by the volume hologram is a spatiospectral mapping between points in the object and points on the detector. As we will see in Section IV-C, the so-called "degeneracy" properties [37] of the volume hologram provide this mapping; the recording geometry is the tool that allows the designer to shape the map structure. The most general usage of volume holograms for imaging is by way of mixing the modes of the field generated by the object with the modes of the hologram through the effect of volume diffraction. Whereas the previous examples can be classified as subcategories of modal imaging, volume holography allows arbitrary shaping the coherence properties of the scattered field. The formal development of this design technique is given in Section V.

B. Imaging System Design

The impact of design choices in individual optical components on system performance is a critical issue for 3-D imaging system design. Lens behavior, for example, has been well characterized in a large variety of imaging conditions, and lens design is an art in itself. Confocal microscopy, along with a large number of high-performance imaging techniques, make good use of advances in lens design. On the other hand, in lensless imaging systems (such as coherence imaging, mentioned above), one tries to get away from the complexity of lens design by using simpler elements (mirrors, prisms) to form interference patterns, and subsequently one uses the computational power of digital computers to apply transformations (Fourier transforms, Fresnel transforms, and possibly nonlinearities) on the detected image intensity in order to recover the 3-D object. With the exception of digital computations, the design of all other imaging system elements is constrained by machining accuracy limitations. Digital transformations themselves are limited by the requirement of reasonable computation time. Therefore, part of the imaging design problem is to achieve a successful balance in splitting the imaging transformations to analog ones, performed by the optical elements, and digital ones, performed by computers, according to the individual capabilities of each component.

A class of optical elements that allow considerable flexibility in their optical response is, of course, holograms. A hologram is determined either by the profiles of the two optical beams that interfere to record it or can be fabricated by etching a waveform on a suitable material (typically glass). In either case, several sophisticated devices are available for determining the hologram response. For example, in the former case, SLM technology allows spatial amplitude and phase modulation of optical beams to resolution down to 10 μm; in the latter, photolithography and electron beam patterning have been used to generate very sophisticated diffractive optical elements for communications, display, and other applications. Holograms have not been very popular as optical elements in practical imaging systems. A notable exception is holographic interferometry [117] and two-wavelength interferometry [118], [119], where the hologram does not function as a fixed imaging element, but rather as a sophisticated detector that captures phase properties of the object. Bertero and collaborators [120]–[126] have proposed a method of superresolving confocal microscopy using diffractive elements calculated based on singular system theory.

We propose to use volume holograms as optical imaging elements for one main reason: a volume element provides a larger number of degrees of freedom in defining the optical response, compared to a surface element (e.g., a thin hologram) of the same aperture. This is intuitively obvious from dimensional arguments and was proven formally in [127] and [128] using the modal properties of electromagnetic fields. We will not repeat the formal arguments here but point out the desirable and undesirable features of volume holography that should be taken into account in the design process. The main price to pay for the advanced design flexibility is that the control problem of defining the hologram response (i.e., "programming" the volume hologram) becomes considerably more difficult and

is accomplished at the expense of diffraction efficiency [128]. Other considerations that follow from the description of Section II are:

1) volume holography provides enormous storage capacity; therefore, a large number of degrees of freedom is available to the designer for shaping the optical response and improving the quality of the image;
2) the capacity goal should be achieved by using as small a number of holograms as possible in order to maintain high individual diffraction efficiency for each hologram;
3) the recording of volume holograms is an expensive, material-limited process that should not be performed in real time; it is better, therefore, to use volume holograms as fixed elements that have been predesigned, fabricated in the factory, and delivered to the user, rather than as dynamic elements modifiable in real time.

What function should the volume hologram perform inside an optical imaging system? Unlike other optical elements, the range of possible responses by volume holograms allows them to perform several functions. We conclude this section by giving an example of a volume hologram as part of a confocal imaging system. The more complicated nature of the hologram's response is fully developed in Section IV-C for several recording geometries. In these cases, the volume hologram acts as a local imaging system by isolating specific light contributions arising from spatial and spectral bands of the object and mapping them onto a 2-D detector. At the end of Section V we will see that a volume hologram may also be designed to act as a global imaging instrument that forms correlations between the light modes emitted (or scattered) by the object and the modes of the hologram.

C. Example: Confocal Imaging with a Volume Holographic Collector

Consider again the confocal imaging system of Fig. 4. The most common performance measure of such a system is "resolution"; i.e., the size of the minimum resolvable element within the object volume. This is equivalent to the volume where the 3-D-PSF of the confocal imaging takes significant values. Ideally, the 3-D PSF is a δ function and the resolution is infinite, but in real-life systems it is nonzero over a finite volume. The confocal arrangement achieves a tight 3-D PSF by: 1) illuminating the point of interest inside the object (the target) by a tightly focused beam, produced by the objective lens, and 2) re-imaging through the collector lens the radiation from the target onto a small pinhole aperture in front of the detector. Thus, point radiators other than the target are doubly inhibited: 1) they are illuminated by an extended low-intensity beam, whereas the target is illuminated by the high-intensity beam waist and 2) the radiation they produce is rejected by the 3-D PSF of the collector because they are away from the focal point.

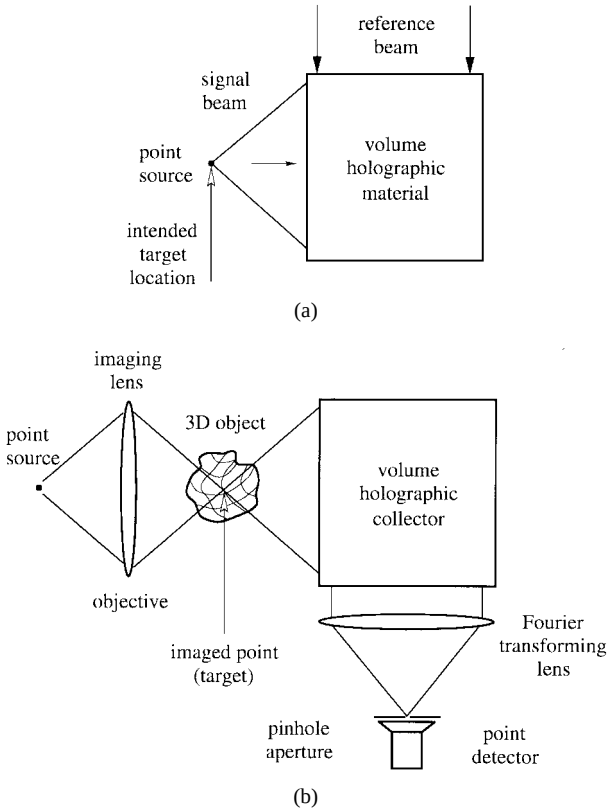

Fig. 6. Confocal imaging arrangement with the collector lens replaced by a volume hologram and a Fourier transforming lens: (a) geometry for recording the volume hologram and (b) confocal imaging arrangement.

Consider now the modified confocal imaging system of Fig. 6(b), where the collector has been replaced by a volume hologram and a Fourier-transforming lens. The volume hologram has been recorded by the interference of a spherical wave originating from the intended target location, and a plane wave oriented normally with respect to the optic axis of the spherical wave, as shown in Fig. 6(a). This recording arrangement is known as "90° geometry," and has been popular in a number of holographic storage demonstrations [5], [6], [22]–[24]. In our imaging configuration [Fig. 6(b)], the volume hologram captures the radiation emitted by the object after illumination by the focused input beam produced by the objective. The diffracted light propagates in the direction shown in Fig. 6(b) and is then captured and Fourier transformed by the lens. The pinhole-sized detector is placed at the focal point of the lens, i.e., it captures the dc component of the diffracted field.

Formally, the volume hologram+lens arrangement forms the correlation between the field emitted by the object and the original signal beam [the spherical wave of Fig. 6(a)]. Radiation emitted from the target position at the recording wavelength is identical to the recording signal and is reconstructed on the detector. Radiation emitted from different positions and at different wavelengths (if the object happens to be polychromatic) does not correlate well with the recording signal and is not reconstructed. The calculation of the diffracted field as a function of the reconstructing object

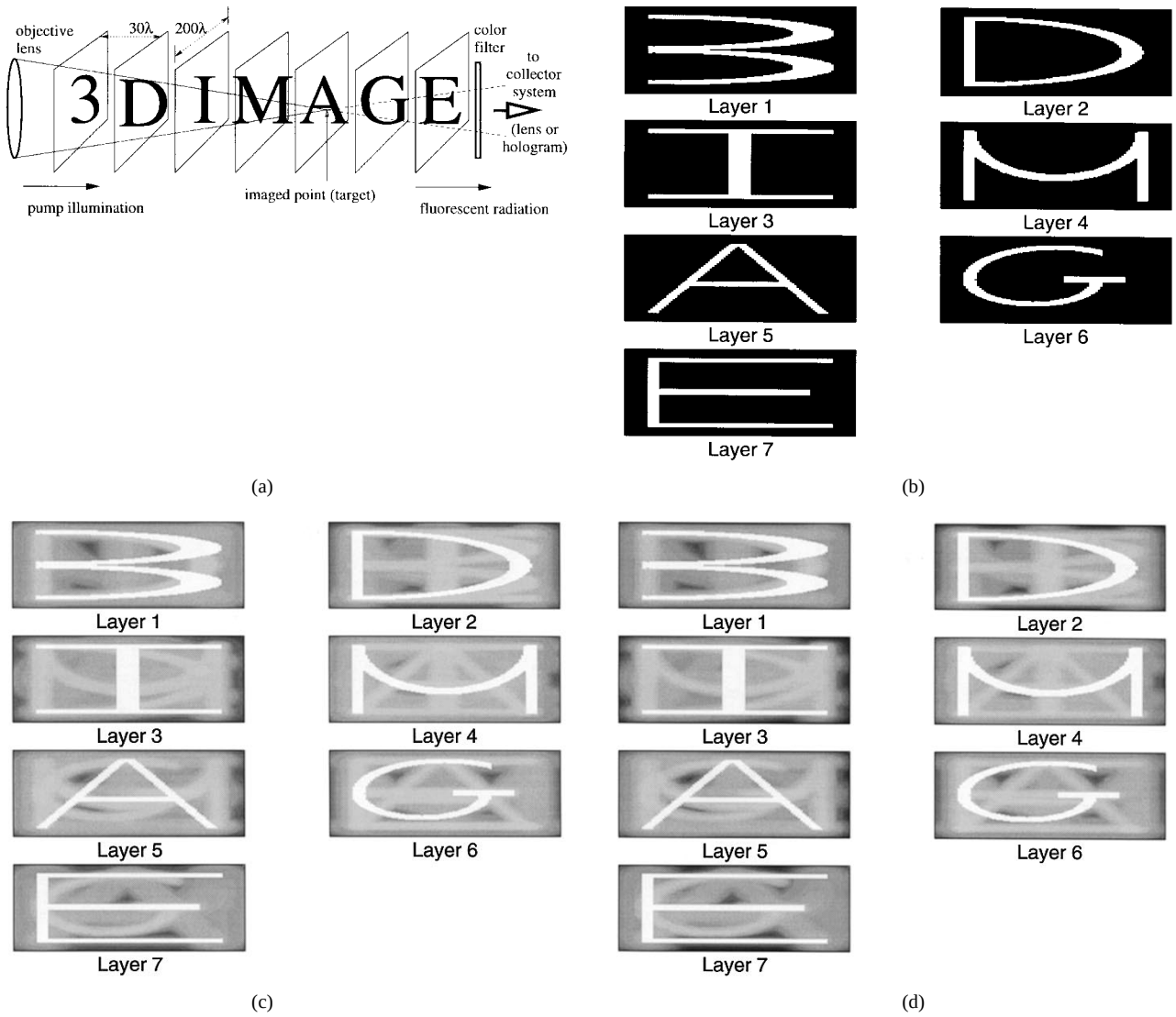

Fig. 7. Numerical comparison of fluorescence confocal imaging with a lens collector and volume holographic collector. For simplicity, the fluorescence wavelength is taken to be equal to the probe wavelength. (a) Geometry used in the simulation. Each plane is modeled as a 100×100 grid of incoherent radiators at the same wavelength λ. (b) Shape of the original object. (c) Fluorescence confocal reconstruction using a lens collector of aperture radius 1500λ, located 2500λ from the plane of the letter "M." (d) Fluorescence confocal reconstruction using a volume holographic collector with aperture radius 1500λ, thickness 3000λ, with its center located 2500λ from the plane of the letter "M."

for this geometry is given in detail in Section IV-B. There we will find out that some parts of the uncorrelated radiation actually are reconstructed, but not at the focal point of the lens. Detecting these reconstructions in an organized way allows the performing of interesting slicing operations on the object. These will be explained in Section IV-C. For the purposes of this section, it suffices to note that, in isolating the radiation emanating from the target point and rejecting the rest, the volume holographic collector is more efficient than an equivalent lens collector. The reason is understood immediately upon comparing the 3-D PSF's of the confocal arrangement with a lens collector as opposed to a volume hologram. The 3-D-PSF calculation is performed using volume diffraction theory in Section IV-B. There, it is shown that the width of the main lobe is the same in both cases; however, the sidelobes are significantly suppressed in the case of the volume holographic collector.

A numerical example demonstrating the importance of the side-lobes is given in Fig. 7. In this example, we numerically reconstructed a fluorescent 3-D incoherent object with the two cases of confocal microscope with a regular lens and volume holographic collector. The resolution was close to the borderline resolution allowed by the numerical aperture of the lens collector. From the reconstructions we see that the lens collector accumulates noise from power diffracted by the sidelobes; this is absent from the volume holographic reconstruction. The signal-to-noise ratios, computed as the quadratic error between object and image normalized to the total image intensity, were $\approx$1500 and $\approx$3500, respectively, for the lens and volume

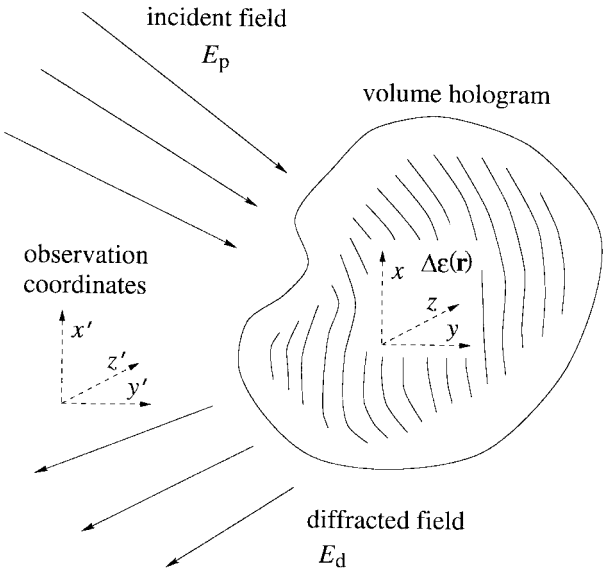

Fig. 8. Schematic of a generic volume diffraction geometry. The probe field $E_p(\mathbf{r})$ and index modulation $\Delta\epsilon(\mathbf{r})$ are expressed in the xyz coordinate system. For notational clarity, we use a different $x'y'z'$ coordinate system for the diffracted field $E_d(\mathbf{r})$.

holographic collector. This improvement is not dramatic, but the design can be combined with matched filtering similar to Bertero's decomposition method [120]–[126], yielding even better results. This last step is not described in this paper.

IV. Diffraction Properties of Volume Holograms with Spherical Reference

As we discussed in Section II, in most holographic materials the recording of a volume hologram is accomplished through modulation of the refractive index. This is expressed as a function $\Delta\varepsilon(\mathbf{r})$ of the space coordinate $\mathbf{r}$, for $\mathbf{r} \in V_{\mathcal{H}}$, where $V_{\mathcal{H}}$ is the volume occupied by the holographic material. A generalized version of the volume diffraction geometry, valid for all the calculations of this section, is given in Fig. 8. When the hologram is illuminated by a probe field $E_p(\mathbf{r})$, the diffracted field $E_d(\mathbf{r}')$ is found as the solution to Maxwell's equations in an inhomogeneous medium, with refractive index as given above. The solution is simplified if we assume that the magnitude of the modulation is much smaller than the unmodulated refractive index ε_0

$$|\Delta\varepsilon(\mathbf{r})| \ll \varepsilon_0, \qquad \mathbf{r} \in V_{\mathcal{H}} \tag{3}$$

because the weak diffraction approximation (also known as "Born's approximation") can then be applied. The diffracted field is given by

$$E_d(\mathbf{r}') = \iiint_{V_{\mathcal{H}}} E_p(\mathbf{r})\Delta\varepsilon(\mathbf{r}) \times \frac{\exp\{ik|\mathbf{r}-\mathbf{r}'|\}}{|\mathbf{r}-\mathbf{r}'|}\, d^3\mathbf{r} \tag{4}$$

where $k = 2\pi/\lambda$ is the wavenumber and the last term in the integrand is recognized as the scalar Green's function for free space. The derivation of (4) from Maxwell's equations is beyond the scope of this paper.

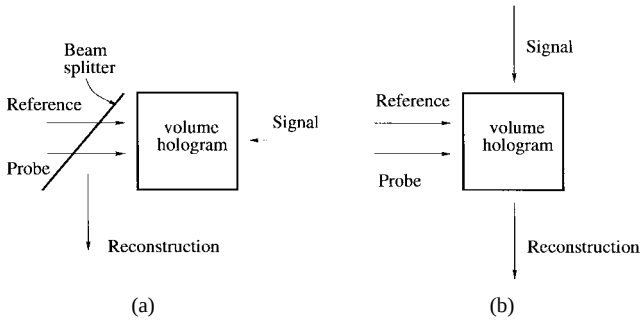

Fig. 9. Simplified holographic recording geometries considered in this paper: (a) reflection geometry and (b) 90° geometry. The reference and probe beams are always spherical waves. We cover both cases when the signal is either spherical wave or a plane wave for (a) in Sections IV-A and IV-C and the case of plane wave signal only for (b) in Sections IV-B and IV-C. The reconstructed beam depends on the relative position and wavelength of the reference and probe beams, the nature of the signal beam, and the shape of the hologram.

Equation (4) has a simple interpretation. Assume that the volume grating is composed of infinitesimal scatterers, the strength of the scatterer located at $\mathbf{r} \in V_{\mathcal{H}}$ being $\Delta\varepsilon(\mathbf{r})$. Then the diffracted field is the coherent summation of the fields emitted by all the scatterers when they are excited by the incident field $E_p(\mathbf{r})$. Naturally, this picture omits higher order scattering, i.e., fields generated when the field scattered from one infinitesimal scatterer reaches other infinitesimal scatterers. This omission, though, is consistent with the weak scattering approximation, which says that these higher order effects are even weaker and, therefore, negligible.

Expression (4) is computationally efficient when spherical waves are involved in the recording of the hologram, as we will see in the next two sections. For other types of fields, a representation of the diffracted field and the grating in wave-vector space works better but is beyond the scope of this paper. For a more complete treatment, the reader is referred to [129].

We will be examining two volume holographic geometries, shown in Fig. 9. In the "reflection geometry" [Fig. 9(a)] the reference and signal beams are incident on two opposite faces of the holographic material and (approximately) counterpropagating. Upon reconstruction, the probe beam is incident in the direction of the reference and the diffracted beam is generated as extension of the signal, i.e., it is counterpropagating, on the same side of the medium as the probe beam. A beam splitter is used to separate the reconstruction from the probe. In the "90° geometry" [Fig. 9(b)] the reference and signal beam are incident on two normal faces of a cube-like recording medium. Again, the probe is incident from the same direction as the reference, and the reconstruction appears as a continuation of the signal, but no beam splitter is required in this geometry.

In the next two sections, we derive the basic formulas that give the diffracted field as function of the output coordinates $\mathbf{r}'$, the recording beams and the geometry of the hologram, for the reflection and 90° geometry, respectively.

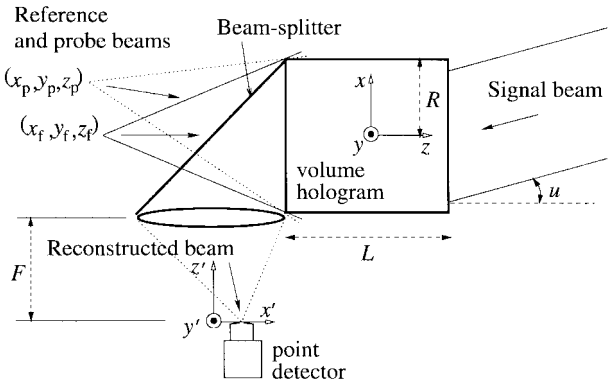

Fig. 10. Schematic of the reflection geometry with spherical wave reference and plane wave signal beams.

In Section IV-C we solve for the locus of probe points and wavelengths that generate maximum reconstructed intensity in the (arbitrarily defined) output plane. The resulting construction is called the "degeneracy surface" of the volume hologram and is important because it specifies the portion of the object that is "visible" by the hologram for imaging purposes.

A. Reflection Holograms

First we consider the geometry of Fig. 10, with a *plane wave* signal beam. The reference beam used for recording is a spherical wave at wavelength λ_f produced by a point source at $\mathbf{r}_f = x_f\hat{\mathbf{x}} + y_f\hat{\mathbf{y}} + z_f\hat{\mathbf{z}}$. We express this wave in the paraxial approximation, as

$$E_f(\mathbf{r}) = \exp\left\{i2\pi\frac{z-z_f}{\lambda_f} + i\pi\frac{(x-x_f)^2+(y-y_f)^2}{\lambda_f(z-z_f)}\right\}. \tag{5}$$

Note that we have neglected a term of the form $1/\lambda(z-z_f)$ because it varies with z much slower than the exponential term. Such slowly varying terms will be neglected from here on. The signal beam is a plane wave propagating at angle $u \ll 1$ with respect to the $\hat{\mathbf{z}}$ axis. In the paraxial approximation, it is expressed as

$$E_s(\mathbf{r}) = \exp\left\{-i2\pi\left(1-\frac{u^2}{2}\right)\frac{z}{\lambda} + i2\pi u\frac{x}{\lambda}\right\}. \tag{6}$$

The modulation of the material refractive index resulting from exposure to beams E_f, E_s given by

$$\Delta\varepsilon(\mathbf{r}) = |E_f(\mathbf{r}) + E_s(\mathbf{r})|^2. \tag{7}$$

Out of the four terms in the interference pattern, we will insert only $E_f^*(\mathbf{r})E_s(\mathbf{r})$ in the volume diffraction equation (4) for the remainder of this section. The remaining three terms are Bragg mismatched and do not diffract significantly.

The probe field is a spherical wave at wavelength λ_p emanating at $\mathbf{r}_p = x_p\hat{\mathbf{x}} + y_p\hat{\mathbf{y}} + z_p\hat{\mathbf{z}}$. The expression for the probe field is

$$E_p(\mathbf{r}) = \exp\left\{i2\pi\frac{z-z_p}{\lambda_p} + i\pi\frac{(x-x_p)^2+(y-y_p)^2}{\lambda_p(z-z_p)}\right\}. \tag{8}$$

To find the diffracted field at the detector coordinates $\mathbf{r}'$ (located near the focus $\mathbf{r}_s$ of the signal beam) we will use Born's diffraction formula (4). We simplify by assuming that the holographic medium is disk shaped with radius R in the xy plane, and thickness L along the z direction, and making the paraxial approximation, i.e., assume that R is smaller than any longitudinal distance that the fields propagate. We then obtain

$$E_d(\mathbf{r}'') = \iiint E_p(\mathbf{r})\Delta\varepsilon(\mathbf{r})\ \mathrm{circ}\left(\frac{\sqrt{x^2+y^2}}{R}\right)\mathrm{rect}\left(\frac{z}{L}\right) \cdot \exp\left\{i2\pi\frac{z''-z}{\lambda_p} + i\pi\frac{(x''-x)^2+(y''-y)^2}{\lambda_p(z''-z)}\right\}\mathrm{d}^2\mathbf{r}. \tag{9}$$

The field reaching the detector is obtained after a Fourier-transforming operation applied by the lens on $E_d(\mathbf{r}'')$, i.e.,

$$\tilde{E}_d(\mathbf{r}') = \iint_{-\infty}^{+\infty} E_d(\mathbf{r}'') \cdot \exp\left\{-i2\pi\frac{x'x''+y'y''}{\lambda_p F}\right\}\mathrm{d}x''\,\mathrm{d}y'' \tag{10}$$

where F is the focal length of the lens and constant phase factors have been omitted. The limits of integration in (10) are taken to be infinite by assuming that the aperture of the Fourier transforming lens is larger than the effective aperture imposed on the diffracted field by the transverse size R of the volume hologram. In other words, we assume that the volume hologram defines the aperture of the system. Under this condition, we can substitute (9) into (10) and perform the x'', y'' integrations right away, obtaining

$$\tilde{E}_d(\mathbf{r}') = \iiint \exp\{i\pi A(z)(x^2+y^2)\} \cdot \exp\{-i2\pi[B_x(z)x + B_y(z)y]\} \cdot \exp\{i\pi C(z)\}\ \mathrm{circ}\left(\frac{\sqrt{x^2+y^2}}{R}\right) \cdot \mathrm{rect}\left(\frac{z}{L}\right)\mathrm{d}^2\mathbf{r} \tag{11}$$

where the coefficients $A(z)$, $B_x(z)$, $B_y(z)$, $C(z)$ are given by

$$A(z) = \frac{1}{\lambda_p(z-z_p)} - \frac{1}{\lambda_f(z-z_f)} \tag{12}$$

$$B_x(z) = -\frac{x_p}{\lambda_p(z-z_p)} + \frac{x_f}{\lambda_f(z-z_f)} - \frac{x'}{\lambda_p F} + \frac{u}{\lambda_f} \tag{13}$$

$$B_y(z) = -\frac{y_p}{\lambda_p(z-z_p)} + \frac{y_f}{\lambda_f(z-z_f)} - \frac{y'}{\lambda_p F} \tag{14}$$

$$C(z) = \frac{x_p^2+y_p^2}{\lambda_f(z-z_p)} - \frac{x_f^2+y_f^2}{\lambda_f(z-z_f)} + \left[4\left(\frac{1}{\lambda_p}-\frac{1}{\lambda_f}\right) - \frac{x'^2+y'^2}{\lambda_p F^2} + \frac{u^2}{\lambda_f}\right]z. \tag{15}$$

To simplify the integral (11), we use the following cylindrical coordinates:

$$\begin{cases} x = \rho\cos\phi, & B_x(z) = B(z)\cos\alpha(z) \\ y = \rho\sin\phi, & B_y(z) = B(z)\sin\alpha(z) \end{cases} \tag{16}$$

with the inverse transformations given by

$$\begin{cases} \rho = \sqrt{x^2+y^2}, & B(z) = \sqrt{B_x(z)^2 + B_y(z)^2} \\ \tan\phi = y/x, & \tan\alpha(z) = B_y(z)/B_x(z) \end{cases} \tag{17}$$

where the sign of the inverse tangent is taken to conform with the quadrant of x, y, and $B_x(z)$, $B_y(z)$, respectively. Equation (11) then becomes

$$\tilde{E}_{\rm d}(\mathbf{r}') = \int_{-L/2}^{L/2} \exp\{i\pi C(z)\} \int_0^R \exp\{i\pi A(z)\rho^2\} \cdot \int_{-\pi}^{\pi} \exp\{-i2\pi B(z)\rho\cos(\phi - \alpha(z))\}\mathrm{d}\phi\rho\mathrm{d}\rho\mathrm{d}z. \tag{18}$$

The result for the innermost integral is well known, expressed in terms of the zero-order Bessel function of the first kind as

$$\int_{-\pi}^{\pi} \exp\{-i2\pi B(z)\rho\cos(\phi - \alpha(z))\}\,\mathrm{d}\phi = 2\pi J_0(2\pi B(z)\rho). \tag{19}$$

The next-level integral occurs in the calculation of the 3-D PSF of a lens near focus, and is written as

$$\int_0^1 \exp\left\{-\frac{i}{2}u\rho^2\right\} J_0(v\rho)\rho\,\mathrm{d}\rho = \mathcal{L}(u,v) \tag{20}$$

where the real and imaginary parts of the function $\mathcal{L}(u,v)$ are expressed in terms of the Lommel functions. For more details, the reader may consult [130, Section 8.8, pp. 435–449]. In terms of the $\mathcal{L}$ function, the diffracted field at the detector is expressed as

$$\tilde{E}_{\rm d}(\mathbf{r}') = 2\pi R^2 \int_{-L/2}^{L/2} \exp\{i\pi C(z)\} \cdot \mathcal{L}\big(2\pi A(z)R^2, 2\pi B(z)R\big)\,\mathrm{d}z. \tag{21}$$

The last integral is calculated numerically. Some properties of the volume hologram are now apparent qualitatively.

1) If the hologram is reconstructed at the recording wavelength ($\lambda_{\rm p} = \lambda_{\rm f}$), with a probe source at the same location as the reference source ($\mathbf{r}_{\rm p} = \mathbf{r}_{\rm f}$), and the detector is placed at the maximum of the Fourier transform of the signal ($x'/F = u$, $y'/F = 0$), then all the exponents in (18) vanish, and the reconstructed power is maximum. This condition is known as Bragg matching.
2) If either the reconstruction wavelength or the probe location change, the detector point $x'/F = u, y'/F = 0$ does not receive maximum power anymore. If the power drops uniformly over the entire detector plane, we say that the hologram is Bragg mismatched. When $\lambda_{\rm p}$ and $\mathbf{r}_{\rm p}$ satisfy certain conditions, though, then significant power is diffracted into some other point on the detector plane ($x'/F \neq u$ or $y'/F \neq 0$). The locus of ($\lambda_{\rm p}$, $\mathbf{r}_{\rm p}$) over which this is possible is the degeneracy surface of the volume hologram. This effect and how it can be used to extract tomographic slices of polychromatic volume objects are the topics of Section IV-C.
3) Since $\mathcal{L}(\cdot,\cdot)$ describes the amplitude transmitted from a quadratic lens also, our result (21) shows that the diffracted light from the volume hologram is the coherent superposition of several "lenses" stacked in the $\hat{\mathbf{z}}$ direction. If the probe source is at the common front focus of all these virtual "lenses," then the "lenses" are all in phase and give a strong reconstruction in the back focal point (Bragg matched case). If the probe moves around or changes its color, the "lens" contributions will in general be out of phase (Bragg-mismatched case), except if the combination of probe position and wavelength and observation position are arranged such that the "lens stack" contributions are again in phase (degeneracy case).

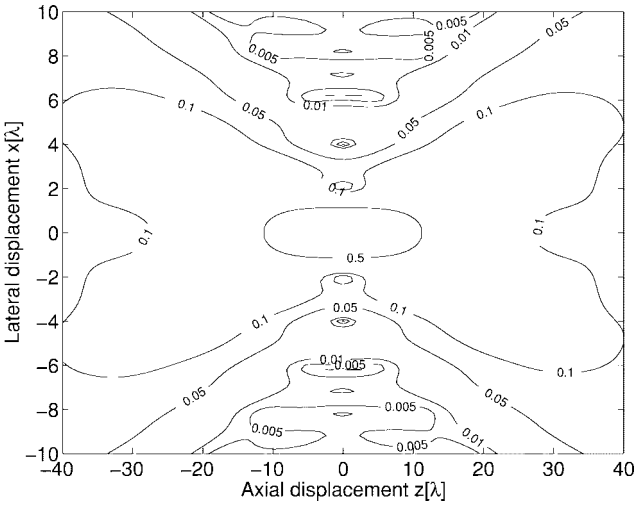

Fig. 11. Contour plot of the diffracted intensity measured by a detector at the focal point $x'/F = y'/F = 0$ of the geometry of Fig. 10, from a point source at position $\mathbf{r}_{\rm p} = (x_{\rm p}, 0, z_{\rm p})$ illuminating a volume hologram with $R = 750\lambda, L = 1500\lambda$. The same diffraction contour plot is obtained also from the geometries of Figs. 13 and 14.

The diffracted power received by a fixed detector pixel $(x'/F, y'/F)$ when $\lambda_{\rm p} = \lambda_{\rm f}$, $y_{\rm p} = 0$ are kept fixed and $x_{\rm p}$, $z_{\rm p}$ are allowed to vary are plotted in Fig. 11. This response, which is common to other recording geometries as well (see below), should be compared with Fig. 12, which is the transmitted intensity captured by the detector if the volume hologram is replaced by a lens of the same aperture as function of $x_{\rm p}$, $z_{\rm p}$. The comparison explains, e.g., why the volume hologram is more efficient as a collector in a confocal microscope arrangement (Section III-C).

Now consider the case of a reflection hologram recorded with a spherical wave signal beam. The geometry is drawn in Fig. 13. The signal beam is now a spherical wave coun-

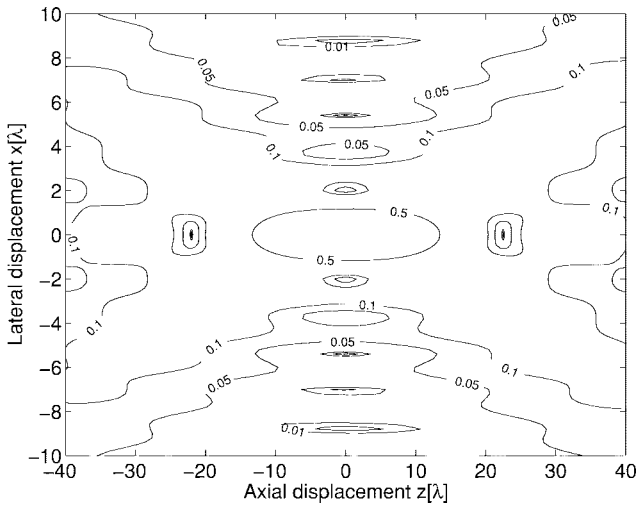

Fig. 12. Contour plot of the transmitted intensity, measured by a detector at the focal point of a thin quadratic lens with aperture $R = 750\lambda$, when illuminated from a point source at position $\mathbf{r}_\mathrm{p} = (x_\mathrm{p}, 0, z_\mathrm{p})$. This plot is, within scaling factors, the same as [130, Fig. 8.41] and is provided for comparison with Fig. 11.

terpropagating with respect to the reference, and coming to a focus at $\mathbf{r}_\mathrm{s} = x_\mathrm{s}\hat{\mathbf{x}} + y_\mathrm{s}\hat{\mathbf{y}} + z_\mathrm{s}\hat{\mathbf{z}}$. The expression of the electric field for this wave is

$$E_\mathrm{s}(\mathbf{r}) = \exp\left\{i2\pi\frac{z-z_\mathrm{s}}{\lambda_\mathrm{f}} + i\pi\frac{(x-x_\mathrm{s})^2+(y-y_\mathrm{s})^2}{\lambda_\mathrm{f}(z-z_\mathrm{s})}\right\}. \tag{22}$$

To find the diffracted field, we start with an expression similar to (9) with (22) substituted in the refractive index modulation $\Delta\epsilon(\mathbf{r}) = E_\mathrm{f}^*(\mathbf{r})E_\mathrm{s}(\mathbf{r})$ and proceed as in the plane-wave signal case, omitting the Fourier-transform step since there is no lens in the arrangement of Fig. 13. The result is

$$E_\mathrm{d}(\mathbf{r}') = 2\pi R^2 \int_{-L/2}^{L/2} \exp\{i\pi C(z)\} \cdot \mathcal{L}(2\pi A(z)R^2, 2\pi B(z)R)\,\mathrm{d}z \tag{23}$$

i.e., identical to (21), but with

$$A(z) = \frac{1}{\lambda_\mathrm{p}(z-z_\mathrm{p})} + \frac{1}{\lambda_\mathrm{p}(z-z')} - \frac{1}{\lambda_\mathrm{f}(z-z_\mathrm{f})} - \frac{1}{\lambda_\mathrm{f}(z-z_\mathrm{s})} \tag{24}$$

$$B_x(z) = -\frac{x_\mathrm{p}}{\lambda_\mathrm{p}(z-z_\mathrm{p})} - \frac{x'}{\lambda_\mathrm{p}(z-z')} + \frac{x_\mathrm{f}}{\lambda_\mathrm{f}(z-z_\mathrm{f})} + \frac{x_\mathrm{s}}{\lambda_\mathrm{f}(z-z_\mathrm{s})} \tag{25}$$

$$B_y(z) = -\frac{y_\mathrm{p}}{\lambda_\mathrm{p}(z-z_\mathrm{p})} - \frac{y'}{\lambda_\mathrm{p}(z-z')} + \frac{y_\mathrm{f}}{\lambda_\mathrm{f}(z-z_\mathrm{f})} + \frac{y_\mathrm{s}}{\lambda_\mathrm{f}(z-z_\mathrm{s})} \tag{26}$$

$$C(z) = \frac{x_\mathrm{p}^2+y_\mathrm{p}^2}{\lambda_\mathrm{f}(z-z_\mathrm{p})} + \frac{x'^2+y'^2}{\lambda_\mathrm{p}(z-z')} - \frac{x_\mathrm{f}^2+y_\mathrm{f}^2}{\lambda_\mathrm{f}(z-z_\mathrm{f})} - \frac{x_\mathrm{s}^2+y_\mathrm{s}^2}{\lambda_\mathrm{f}(z-z_\mathrm{s})} + 4\left(\frac{1}{\lambda_\mathrm{p}} - \frac{1}{\lambda_\mathrm{f}}\right)z. \tag{27}$$

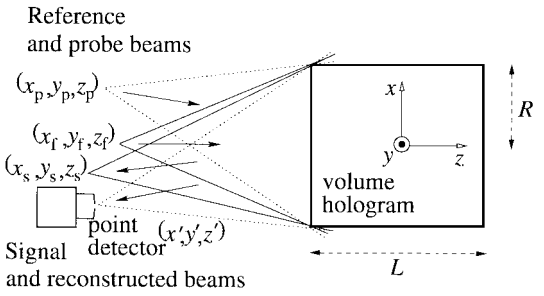

Fig. 13. Schematic of the reflection geometry with spherical wave reference and signal beams.

The plot of diffracted power when λ_p, $\mathbf{r}'$ and y_p are fixed, while x_p, z_p vary, is virtually identical to that of Fig. 11 (this can be verified by comparing the expressions for the coefficients and the changes in the exponents as x_p, z_p change), so it will not be given again. The degeneracy surface for this geometry will be calculated in Section IV-C along with the other recording geometries.

B. 90° Geometry Holograms

The 90° geometry differs from the reflection geometry because the paraxial approximation for the signal and diffracted beams is made along the $\hat{\mathbf{x}}$ rather than the $\hat{\mathbf{z}}$ axis. This leads to quantitatively different expressions in the diffraction integrals. We will examine in this section the case of a plane wave signal only, incident at angle $u \ll 1$ with respect to the $\hat{\mathbf{x}}$ axis, as shown in Fig. 14. The reference and signal beams are

$$E_\mathrm{f}(\mathbf{r}) = \exp\left\{i2\pi\frac{z-z_\mathrm{f}}{\lambda_\mathrm{f}} + i\pi\frac{(x-x_\mathrm{f})^2+(y-y_\mathrm{f})^2}{\lambda_\mathrm{f}(z-z_\mathrm{f})}\right\} \tag{28}$$

$$E_\mathrm{s}(\mathbf{r}) = \exp\left\{-i2\pi\left(1-\frac{u^2}{2}\right)\frac{x}{\lambda} + i2\pi u\frac{z}{\lambda}\right\}. \tag{29}$$

For a probe field

$$E_\mathrm{p}(\mathbf{r}) = \exp\left\{i2\pi\frac{z-z_\mathrm{p}}{\lambda_\mathrm{p}} + i\pi\frac{(x-x_\mathrm{p})^2+(y-y_\mathrm{p})^2}{\lambda_\mathrm{p}(z-z_\mathrm{p})}\right\} \tag{30}$$

and an observation point $\mathbf{r}''$ near the $\hat{\mathbf{x}}$ axis, the diffraction integral in the paraxial approximation is given as

$$E_\mathrm{d}(\mathbf{r}'') = \iiint E_\mathrm{p}(\mathbf{r})\Delta\varepsilon(\mathbf{r})\,\mathrm{circ}\left(\frac{\sqrt{x^2+y^2}}{R}\right)\mathrm{rect}\left(\frac{z}{L}\right) \times \exp\left\{i2\pi\frac{x''-x}{\lambda_\mathrm{p}} + i\pi\frac{(y''-y)^2+(z''-z)^2}{\lambda_\mathrm{p}(x''-x)}\right\}\mathrm{d}^3\mathbf{r}. \tag{31}$$

Performing the Fourier transform in y'', z'', and subsequently the integrals in cylindrical coordinates as in Section IV-A for the plane wave case, we obtain yet again a result of the form

$$\tilde{E}_\mathrm{d}(\mathbf{r}') = 2\pi R^2 \int_{-L/2}^{L/2} \exp\{i\pi C(z)\} \cdot \mathcal{L}\big(2\pi A(z)R^2, 2\pi B(z)R\big)\,\mathrm{d}z. \tag{32}$$

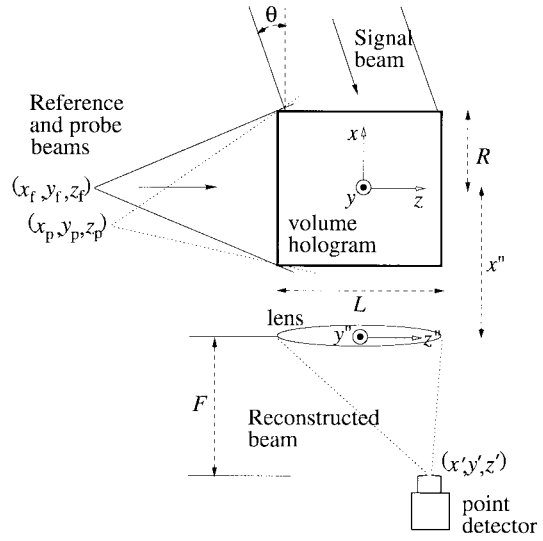

Fig. 14. Schematic of the 90° geometry with spherical wave reference and plane wave signal beams.

This time the coefficients are given by

$$A(z) = \frac{1}{\lambda_p(z - z_p)} - \frac{1}{\lambda_f(z - z_f)} \tag{33}$$

$$B_x(z) = -\frac{x_p}{\lambda_p(z - z_p)} + \frac{x_f}{\lambda_f(z - z_f)} + \frac{y'^2 + z'^2}{2\lambda_p F^2} - \frac{u^2}{2\lambda_f} + \frac{1}{\lambda_f} - \frac{1}{\lambda_p} \tag{34}$$

$$B_y(z) = -\frac{y_p}{\lambda_p(z - z_p)} + \frac{y_f}{\lambda_f(z - z_f)} - \frac{y'}{\lambda_p F} \tag{35}$$

$$C(z) = \frac{x_p^2 + y_p^2}{\lambda_f(z - z_p)} - \frac{x_f^2 + y_f^2}{\lambda_f(z - z_f)} + 2\left(\frac{u}{\lambda_f} - \frac{z'}{\lambda_p F} + \frac{1}{\lambda_p} - \frac{1}{\lambda_f}\right)z. \tag{36}$$

The change in diffracted power as function of x_p, z_p is, once again, identical to Fig. 11, and will not be given separately. The degeneracies will be calculated immediately below.

C. Hologram Degeneracies and Multispectral Tomography

We now turn to the calculation of the hologram degeneracies, i.e., the conditions for achieving significant reconstructed power even when the probe field is not a replica of the reference field. From the diffraction integrals (21), (23), (32), we can see that the condition for obtaining significant reconstruction is equivalent to setting the arguments of $\mathcal{L}(\cdot,\cdot)$ as well as the varying portion of $C(\cdot)$ equal to zero. If these conditions are not satisfied, the value of the integral decreases, i.e., Bragg mismatch occurs.

Obviously, in each geometry there are several parameters that one may manipulate in order to eliminate the exponents. The selection depends on the application. We are interested in the case of a reconstructing field produced by an extended polychromatic object, and a planar two-dimensional detector located at the exit plane of the system. Then, the parametrization of interest is the locus and wavelength of the point radiators within the object that produce maximum reconstructed power on a particular pixel of the detector as a function of the pixel coordinates on the detector. We will see that this parametrization results, in each case, in a surface in object space; this is the degeneracy surface for our chosen planar detector geometry (nonplanar detector surfaces would yield different degeneracy surfaces but are hard to come about in practice). The reconstructing wavelength must vary across the degeneracy surface, too, for maximum reconstructed power. Thus, the field diffracted off the volume hologram "isolates" a surface subset of radiators in space, as well as filters them in color. This is equivalent to a tomographic slicing operation in both space and spectral domains. By scanning the volume hologram in two dimensions, the full four-dimensional (4-D) reconstruction of the object (in space and color) can be obtained. We now derive the degeneracy surface shapes for various holographic recording geometries, in order to demonstrate the operation of the volume hologram as a spatiospectral filter.

We begin with the case of a plane wave signal, reflection geometry hologram, as in the first part of Section IV-A. For later convenience, we define the parameter $\mu = \lambda_p/\lambda_f$. To derive the degeneracy surface, we set all coefficients $A(z)$, $B_x(z)$, $B_y(z)$, $C(z)$ equal to zero, at least to first order in z. From (12) we obtain

$$z_p = \frac{z_f}{\mu}. \tag{37}$$

From (13), and using (37), follows

$$x_p = x_f + z_f\left(\frac{1}{\mu}\frac{x'}{F} - u\right) \tag{38}$$

whereas (14) and (37) yield

$$y_p = y_f + \frac{z_f}{\mu}\frac{y'}{F}. \tag{39}$$

Substituting into (15) results in the following quadratic equation in μ

$$D\mu^2 + G\mu - H = 0 \tag{40}$$

where

$$D = \left(\frac{x_f}{z_f} - u\right)^2 + \frac{y_f^2}{z_f^2} \tag{41}$$

$$G = 4 - 2u\frac{x_f}{z_f} + \frac{x'^2 + y'^2}{F^2} - \left(\frac{x_f}{z_f} - u - \frac{x'}{F}\right)^2 - \left(\frac{y_f}{z_f} - \frac{y'}{F}\right)^2 \tag{42}$$

$$H = 4 - 2\frac{x'^2 + y'^2}{F^2}. \tag{43}$$

Therefore, the degeneracy surface is obtained by setting μ equal to the root of (40) that is closest to 1 in magnitude and then substituting in (37)–(39). The result for a particular

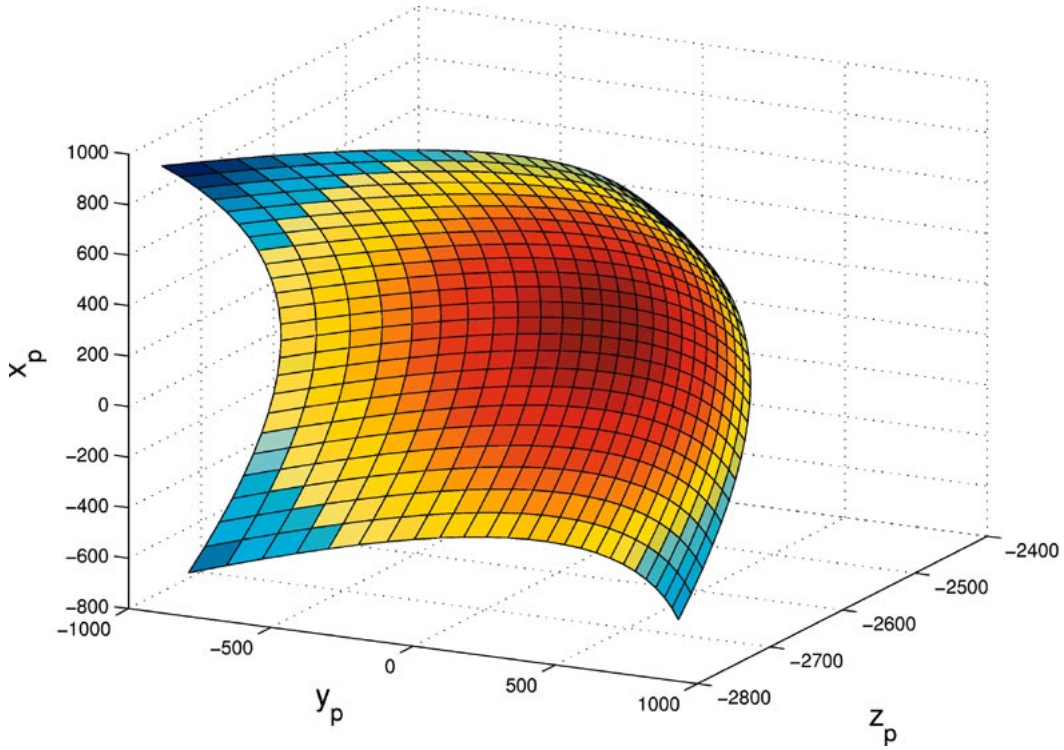

Fig. 15. Degeneracy surface (space and color) of the reflection recording geometry with a plane wave signal, computed numerically. The parameters for this plot were $\mathbf{r}_f = (100, -100, -2500)\lambda$, $u = 0, -0.3 \leq x'/F, y'/F \leq 0.3$. In the plot, the blue color corresponds to $\mu = 0.899$ and the purple to $\mu = 1.0$.

numerical example is shown in Fig. 15. Two important points about the surface of Fig. 15 should be noted.

1) The degeneracy surface is not infinitely thin as implied by the drawing but has a finite thickness because the reconstructed intensity from points and colors near the surface is not zero but falls off smoothly according to (21).
2) The diffraction efficiency from points belonging to the degeneracy surface is not uniformly 1 but falls off toward the surface edges because higher order z terms in the exponents cause weak Bragg mismatch; this deviation from true degeneracy is also calculated by use of (21).

Numerical results for the surface thickness and deviation from degeneracy are not given here but can be calculated easily. These remarks also hold for the surfaces computed later in this section.

The derivation of the degeneracy surfaces for other recording geometries is similar to the one just described and will not be given here; only the results will be quoted.

For the spherical wave signal reflection geometry case, μ is the root, closest in magnitude to 1, of

$$D\mu^2 + G\mu - H = 0 \tag{44}$$

where

$$D = \left(\frac{x_f}{z_f} + \frac{x_s}{z_s}\right)^2 + \left(\frac{y_f}{z_f} + \frac{y_s}{z_s}\right)^2 \tag{45}$$

$$G = 4 - 2\frac{x_f x_s + y_f y_s}{z_f} + \frac{x'^2 + y'^2}{z'^2} - \left(\frac{x_f}{z_f} + \frac{x_s}{z_s} + \frac{x'}{F}\right)^2 - \left(\frac{y_f}{z_f} + \frac{y_s}{z_s} + \frac{y'}{F}\right)^2 \tag{46}$$

$$H = 4 - 2\frac{x'^2 + y'^2}{F^2}. \tag{47}$$

The spatial coordinates of the degeneracy surface are obtained from

$$\frac{1}{z_p} = \mu\left(\frac{1}{z_f} + \frac{1}{z_s}\right) - \frac{1}{z'} \tag{48}$$

$$\frac{x_p}{z_p} = \mu\left(\frac{x_f}{z_f} + \frac{x_s}{z_s}\right) - \frac{x'}{z'} \tag{49}$$

$$\frac{y_p}{z_p} = \mu\left(\frac{y_f}{z_f} + \frac{y_s}{z_s}\right) - \frac{y'}{z'}. \tag{50}$$

A numerical example is given in Fig. 16. It is interesting to note that the degeneracy surface in this case is identical to the surface obtained in the case of a plane wave signal (derived immediately above) with $x_s = -uz_s$, $y_s = 0$, and inverted output coordinates ($x' \leftrightarrow -x'$, $y' \leftrightarrow -y'$).

For the plane wave signal 90° geometry case, the quadratic equation for μ is also of the form

$$D\mu^2 + G\mu - H = 0 \tag{51}$$

where

$$D = 1 + \frac{x_f^2 + y_f^2}{z_f^2} - 2\frac{x_f}{z_f} - u^2 \tag{52}$$

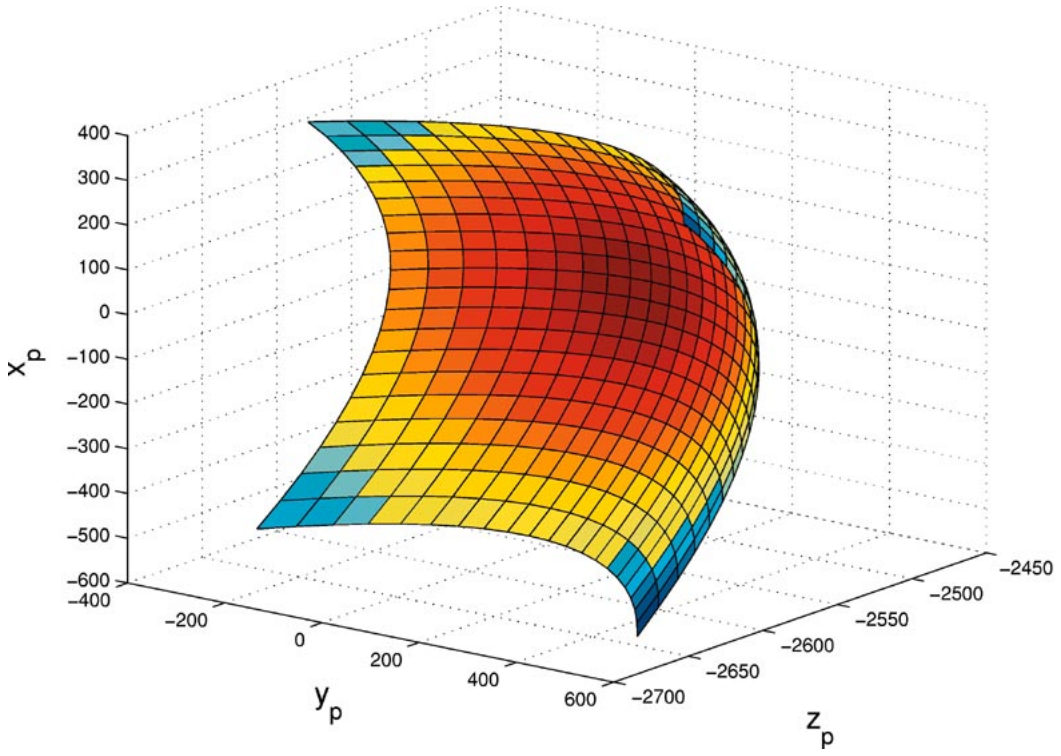

Fig. 16. Degeneracy surface (space and color) of the reflection recording geometry with a spherical wave signal, computed numerically. The parameters for this plot were $\mathbf{r}_{\mathrm{f}} = (-100, 100, -2500)\lambda$, $\mathbf{r}_{\mathrm{s}} = (0, 0, -3000)\lambda$, $-500\lambda \leq x', y' \leq 500\lambda, z' = -3000\lambda$. In the plot, the blue color corresponds to $\mu = 0.966$ and the purple to $\mu = 1.0$.

$$G = \left(1 + \frac{x_{\mathrm{f}}}{z_{\mathrm{f}}}\right)^2 + \left(\frac{y_{\mathrm{f}}}{z_{\mathrm{f}}} + \frac{y'}{F}\right)^2 + \frac{z'^2}{F^2} + (u-1)^2 - 2\left(1 + \frac{x_{\mathrm{f}}^2 + y_{\mathrm{f}}^2}{z_{\mathrm{f}}^2}\right) \tag{53}$$

$$H = \left(1 - \frac{z'}{F}\right)^2. \tag{54}$$

After solving for μ as the root of the quadratic with magnitude closest to 1, the spatial coordinates are obtained from

$$z_{\mathrm{p}} = \frac{z_{\mathrm{f}}}{\mu} \tag{55}$$

$$\frac{x_{\mathrm{p}}}{z_{\mathrm{p}}} = -\mu\left(1 - \frac{x_{\mathrm{f}}}{z_{\mathrm{f}}} - \frac{u^2}{2}\right) + \left(1 - \frac{y'^2 + z'^2}{2F^2}\right) \tag{56}$$

$$\frac{y_{\mathrm{p}}}{z_{\mathrm{p}}} = \mu\frac{y_{\mathrm{f}}}{z_{\mathrm{f}}} + \frac{y'}{F}. \tag{57}$$

A numerical example is given in Fig. 17.

For the sake of completeness, we also give the result for the degeneracy surface of a volume hologram recorded with a spherical wave signal in the 90° geometry (see Fig. 18 for the notation). The calculation of the diffracted field cannot be done under the framework of Sections IV-A and IV-B and will not be given here. However, the degeneracy derivation is straightforward. It results also in a quadratic equation for μ of the form

$$D\mu^2 + G\mu - H = 0 \tag{58}$$

where

$$D = 1 + \frac{x_{\mathrm{f}}^2 + y_{\mathrm{f}}^2}{z_{\mathrm{f}}^2} - 2\left(\frac{x_{\mathrm{f}}}{z_{\mathrm{f}}} + \frac{y_{\mathrm{f}}}{z_{\mathrm{f}}}\,\frac{y_{\mathrm{s}}}{x_{\mathrm{s}}}\right) - \frac{z_{\mathrm{s}}^2}{x_{\mathrm{s}}^2} \tag{59}$$

$$G = \left(1 + \frac{x_{\mathrm{f}}}{z_{\mathrm{f}}}\right)^2 + \left(\frac{y_{\mathrm{f}}}{z_{\mathrm{f}}} + \frac{y'}{x'}\right)^2 + \frac{z'^2}{x'^2} + \frac{y_{\mathrm{s}}^2 + z_{\mathrm{s}}^2}{x_{\mathrm{s}}^2} - 1 - 2\frac{x_{\mathrm{f}}^2 + y_{\mathrm{f}}^2}{z_{\mathrm{f}}^2} - 2\frac{y'y_{\mathrm{s}}}{x'x_{\mathrm{s}}} \tag{60}$$

$$H = 1 + \frac{z'^2}{x'^2}. \tag{61}$$

The spatial coordinates of the degeneracy surface are given by

$$z_{\mathrm{p}} = \frac{z_{\mathrm{f}}}{\mu} \tag{62}$$

$$\frac{x_{\mathrm{p}}}{z_{\mathrm{p}}} = -\mu\left(1 - \frac{x_{\mathrm{f}}}{z_{\mathrm{f}}} - \frac{y_{\mathrm{s}}^2 + z_{\mathrm{s}}^2}{2x_{\mathrm{s}}^2}\right) + \left(1 - \frac{y'^2 + z'^2}{2x'^2}\right) \tag{63}$$

$$\frac{y_{\mathrm{p}}}{z_{\mathrm{p}}} = \mu\left(\frac{y_{\mathrm{f}}}{z_{\mathrm{f}}} - \frac{y_{\mathrm{s}}}{x_{\mathrm{s}}}\right) + \frac{y'}{x'} \tag{64}$$

with μ computed from (58). A numerical example is given in Fig. 19.

V. Statistical Properties of Diffraction from Volume Gratings

In the examples of the previous sections, we made assumptions about the nature of the random objects reconstructing the volume hologram, as well as about the form of the hologram itself. In particular, we worked with volume

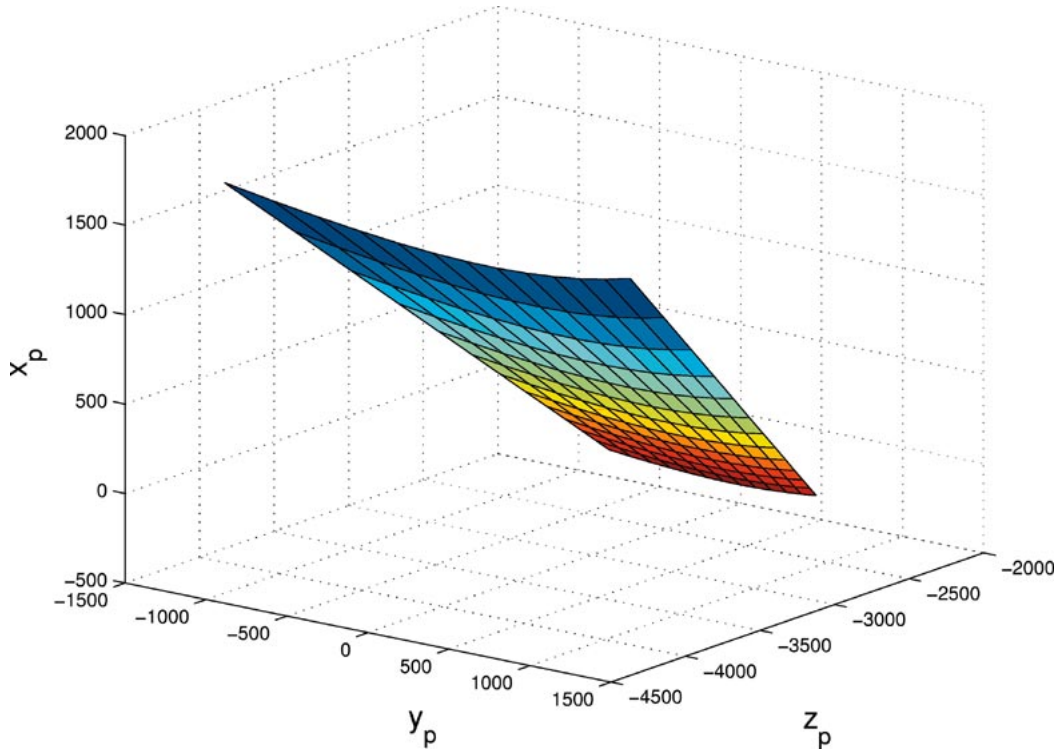

Fig. 17. Degeneracy surface (space and color) of the 90° recording geometry with a plane wave signal, computed numerically. The parameters for this plot were $\mathbf{r}_f = (100, -100, -2500)\lambda$, $u = 0, -0.3 \leq x'/F, y'/F \leq 0.3$. In the plot, the blue color corresponds to $\mu = 0.619$ and the purple to $\mu = 1.246$.

holograms recorded with a spherical reference beam and derived their operation as point-source correlators for imaging under two conditions: 1) when replacing the collector lens in a fluorescent confocal microscope with a monochromatic object (Section III-C), they improve the resolution of the regular confocal arrangement, and 2) when reconstructing a polychromatic (4-D) object, they isolate a surface in the space and wavelength domain, allowing the full 4-D tomographic reconstruction of the object with appropriate scanning (Section IV-C). Color-selective tomography is a unique property of volume holograms as optical elements and cannot be achieved by a design that incorporates planar optical elements only. In this section, we generalize the volume hologram operation as shaping the modes of the object field through correlation (mixing) with the modes of the volume hologram.

As we mentioned already in Section III-A, computational imaging is performed, in general, by transformations on the intensity values of the field at the detector plane. When viewed as an analysis problem, this means that one needs to know the statistical properties of the intensity values at the output plane as a function of the imaging system and the statistics of the object. From the design point of view, it is desired to construct the imaging system so as to shape the output intensity statistics appropriately for the task at hand. The intensity transformation law between the source intensity distribution $I_s(\mathbf{r}')$ and the intensity distribution at the detector space $I_d(\mathbf{r})$ is, in the case of a completely incoherent source, of the form

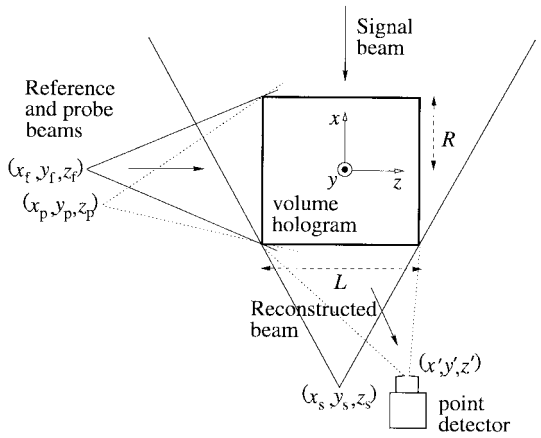

Fig. 18. Schematic of the 90° geometry with sperical wave reference and signal beams.

$$I_d(\mathbf{r}') = \int_{V_S} I_s(\mathbf{r}) h(\mathbf{r}', \mathbf{r})\, d^3\mathbf{r} \tag{65}$$

where the transfer function $h(\mathbf{r}', \mathbf{r})$ describes the operation of the optical system.

In many imaging systems, there is a single optical beam propagating between the object and image. Such was the operation of the volume holographic system of Figs. 6, 10, 13, 14, and 18. We would like to characterize the operation of a volume hologram in configurations where two or more beams interfere on the detector plane. In such

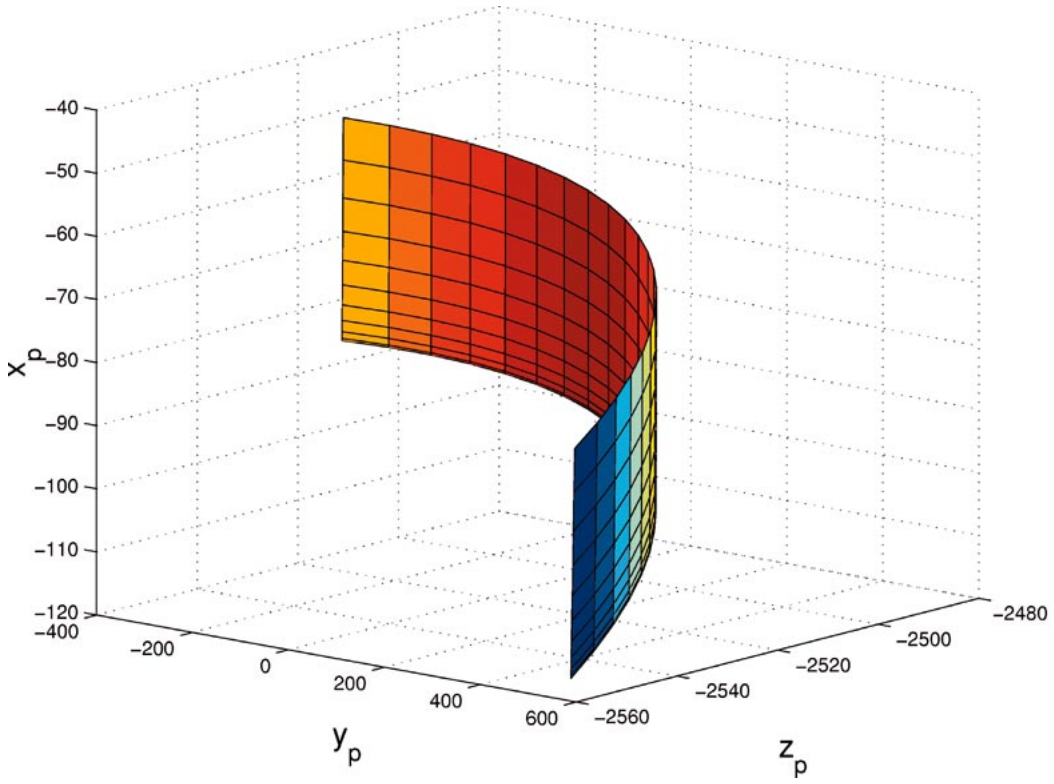

Fig. 19. Degeneracy surface (space and color) of the 90° recording geometry with a spherical wave signal, computed numerically. The parameters for this plot were $\mathbf{r}_{\mathrm{f}} = (-100, 100, -2500)\lambda$, $\mathbf{r}_{\mathrm{s}} = (3000, 0, 0)\lambda$, $-500\lambda \leq y', z' \leq 500\lambda, x' = 3000\lambda$. In the plot, the blue color corresponds to $\mu = 0.979$ and the purple to $\mu = 1.0$.

interferometric systems, the $I_{\mathrm{d}}(\mathbf{r}')$ measurement contains information about the statistical correlation properties of the field at the output. We therefore need to model the effect of volume diffraction on the correlation properties of a random optical field. To this end, in the remainder of this section, we first introduce the notation and terminology of statistical optics [131], [132] and rederive the deterministic correlation property of volume diffraction; we then generalize the correlation property in a statistical framework and use the modal decomposition of both the field coherence function and the hologram refractive index modulation in order to formulate the operation of the volume hologram as a design problem.

Suppose the geometry of an imaging system is such that the fields from two observation points $\mathbf{r}_1'(\mathbf{r}')$, $\mathbf{r}_2'(\mathbf{r}')$ interfere at every point $\mathbf{r}'$ in the detector space. The measurement then is (dropping the $\mathbf{r}'$ dependence of $\mathbf{r}_1'$, $\mathbf{r}_2'$ for notational simplicity)

$$I_{\mathrm{d}}(\mathbf{r}') = \mathrm{E.V.}\{|E_{\mathrm{d}}(\mathbf{r}_1') + E_{\mathrm{d}}(\mathbf{r}_2')|^2\}. \tag{66}$$

Using the definitions

$$I_{\mathrm{d}}(\mathbf{r}_j') = \mathrm{E.V.}\{|E_{\mathrm{d}}(\mathbf{r}_j')|^2\} \qquad j = 1, 2 \tag{67}$$

$$\Gamma_{\mathrm{d}}(\mathbf{r}_1', \mathbf{r}_2', \tau) = \mathrm{E.V.}\{E^*(\mathbf{r}_1', t)E(\mathbf{r}_2', t+\tau)\} \tag{68}$$

where τ is the relative time delay between the two optical paths and Γ_{d} is the second-order correlation function of the random optical field, we obtain for the detected intensity the result

$$I_{\mathrm{d}}(\mathbf{r}') = I_{\mathrm{d}}(\mathbf{r}_1') + I_{\mathrm{d}}(\mathbf{r}_2') + 2\ \mathrm{Re}\ \Gamma_{\mathrm{d}}(\mathbf{r}_1', \mathbf{r}_2', \tau). \tag{69}$$

The last result states that the interferometric measurement contains the field correlation information superimposed on a quasi-uniform bright background (typically, the variation of $I_{\mathrm{d}}(\mathbf{r}_1')$ with $\mathbf{r}_1'$ is very small). Instead of $\Gamma_{\mathrm{d}}(\mathbf{r}_1', \mathbf{r}_2', \tau)$, it is typical to assume that the field is quasi-monochromatic, and that the path delay is $\tau = 0$, and use the mutual intensity $J_{\mathrm{d}}(\mathbf{r}_1', \mathbf{r}_2')$, defined as

$$J_{\mathrm{d}}(\mathbf{r}_1', \mathbf{r}_2') = \Gamma_{\mathrm{d}}(\mathbf{r}_1', \mathbf{r}_2', 0). \tag{70}$$

Relation (69) then becomes

$$I_{\mathrm{d}}(\mathbf{r}') = I_{\mathrm{d}}(\mathbf{r}_1') + I_{\mathrm{d}}(\mathbf{r}_2') + 2\ \mathrm{Re}\ J_{\mathrm{d}}(\mathbf{r}_1', \mathbf{r}_2'). \tag{71}$$

These results are well known and hold for any interferometric optical system; we seek to compute the effect of a volume hologram on the mutual intensity $J_{\mathrm{d}}(\mathbf{r}_1', \mathbf{r}_2')$. Before getting to that point, though, it is useful to repeat a deterministic property of volume diffraction: if a volume hologram is illuminated by a complex (coherent) field, then the diffracted field contains the 2-D correlation between the input field and the pattern(s) stored in the modulated refractive index of the hologram. The generalization to statistical fields is then obvious.

Let $V_{\mathcal{S}}$ be the volume where a three-dimensional monochromatic (at wavelength $\lambda = 2\pi/k$) probe light source is confined, and $E_{\mathrm{p}}(\mathbf{r}'')$ the field emitted by an

infinitesimal source volume at $\mathbf{r}'' \in V_{\mathcal{S}}$. Let $V_{\mathcal{H}}$ be the volume where a 3-D perturbation $\Delta\epsilon(\mathbf{r})$ of the refractive index is confined ($\Delta\epsilon(\mathbf{r}) = 0$ for $\mathbf{r} \notin V_{\mathcal{H}}$), i.e., a volume hologram. When the field scattered by $V_{\mathcal{S}}$ reaches $V_{\mathcal{H}}$, a secondary diffracted field $E_{\mathrm{d}}(\mathbf{r}')$ ($\mathbf{r}' \notin V_{\mathcal{S}}$, $V_{\mathcal{H}}$) is produced. Let $\hat{\mathbf{n}}$ denote a vector of unit magnitude in an arbitrary direction that from here on we refer to as "optical axis." The 3-D spatial spectrum of the source field is denoted as

$$\tilde{E}_{\mathrm{s}}(\mathbf{k}) = \int_{\mathbb{R}^3} E_{\mathrm{s}}(\mathbf{r}) \exp\{-i\mathbf{k}\cdot\mathbf{r}\}\, \mathrm{d}^3\mathbf{r} \tag{72}$$

with a similar expression for $\tilde{E}_{\mathrm{d}}$. We also denote

$$\mathbf{k}_{\perp} = \mathbf{k} \times \hat{\mathbf{n}}, \quad k_{\parallel} = \mathbf{k}\cdot\hat{\mathbf{n}} \qquad \left(|\mathbf{k}_{\perp}|^2 + k_{\parallel}^2 = k^2\right).$$

The correlation property is then expressed as follows:

$$\tilde{E}_{\mathrm{d}}(\mathbf{k}) = \frac{1}{k_{\parallel}}\left(\frac{\tilde{E}_{\mathrm{s}}}{k_{\parallel}} \star \Delta\tilde{\epsilon}^{\star}\right) \tag{73}$$

for $\mathbf{k}$ satisfying $|\mathbf{k}| = k$, where the $\star$ denotes correlation and $\Delta\tilde{\epsilon}^*$ is the complex conjugate of $\Delta\tilde{\epsilon}$. The proof of this statement is given in Appendix I.

The generalization of (73) to a random field is straightforward. We define the spatial Fourier transform of the source mutual intensity function as

$$\tilde{J}_{\mathrm{s}}(\mathbf{k}_1, \mathbf{k}_2) = \iint_{\mathbb{R}^2} J_{\mathrm{s}}(\mathbf{r}_1, \mathbf{r}_2) \cdot \exp\{-i(\mathbf{k}_1\cdot\mathbf{r}_1 + \mathbf{k}_2\cdot\mathbf{r}_2)\}\, \mathrm{d}^2\mathbf{r}_1\, \mathrm{d}^2\mathbf{r}_2 \tag{74}$$

with a similar expression for $\tilde{J}_{\mathrm{d}}(\mathbf{k}_1, \mathbf{k}_2)$. Then, under the constraint $|\mathbf{k}_1| = |\mathbf{k}_2| = k$, $\tilde{J}_{\mathrm{d}}(\mathbf{k}_1, \mathbf{k}_2)$ is related to $\tilde{J}_{\mathrm{s}}(\mathbf{k}_1, \mathbf{k}_2)$ through

$$\tilde{J}_{\mathrm{d}}(\mathbf{k}_1, \mathbf{k}_2) = \iint_{\mathbb{R}^2} \frac{\tilde{J}_{\mathrm{s}}(\boldsymbol{\kappa}_1'', \boldsymbol{\kappa}_2'')}{k_{1,\parallel} k_{2,\parallel} k_{1,\parallel}'' k_{2,\parallel}''} \Delta\tilde{\epsilon}(\boldsymbol{\kappa}_1'' - \mathbf{k}_1) \cdot \Delta\tilde{\epsilon}^*(\boldsymbol{\kappa}_2'' - \mathbf{k}_2)\, \mathrm{d}^2\mathbf{k}_{1,\perp}''\, \mathrm{d}^2\mathbf{k}_{2,\perp}''. \tag{75}$$

Similar to Appendix I, we used the notation $\boldsymbol{\kappa}_j'' = \mathbf{k}_{j,\perp} + \hat{\mathbf{n}}\sqrt{k^2 - |\mathbf{k}_{j,\perp}|^2}$, $j = 1, 2$. The proof of (75) is given in Appendix II. (This expression also follows directly by specializing a result derived in [112] to the case of a volume hologram; the full proof is given here for completeness.) This is also a correlation relation between the six-dimensional functions $\tilde{J}_{\mathrm{d}}(\mathbf{k}_1, \mathbf{k}_2)$ and $\Delta\tilde{\epsilon}^*(\mathbf{k}_1)\Delta\tilde{\epsilon}(\mathbf{k}_2)$ constrained on the 4-D sphere $|\mathbf{k}_1| = |\mathbf{k}_2| = k$.

We now seek to cast (75) as a design problem. To this end, we decompose both the Fourier-transformed mutual intensities $\tilde{J}_{\mathrm{d}}(\mathbf{k}_1, \mathbf{k}_2)$, $\tilde{J}_{\mathrm{s}}(\mathbf{k}_1, \mathbf{k}_2)$ and the index modulation $\Delta\tilde{\epsilon}(\mathbf{k})$ in their respective modes and show how the modes mix as a result of volume diffraction.

The coherent mode decomposition property for a general random field states that, under some general existence and continuity conditions for the cross-spectral density, the quantity $J(\mathbf{r}_1, \mathbf{r}_2)$ can be decomposed into a sum of products of orthogonal modes. For the source field, the decomposition is written as follows:

$$J_{\mathrm{s}}(\mathbf{r}_1, \mathbf{r}_2) = \sum_{\mathbf{m}} \alpha_{\mathbf{m}} \psi_{\mathbf{m}}^*(\mathbf{r}_1)\psi_{\mathbf{m}}(\mathbf{r}_2) \tag{76}$$

where the $\psi_{\mathbf{m}}$ are the eigenfunctions and the $\alpha_{\mathbf{m}}$ the eigenvalues of the Friedholm-type integral equation

$$\int_{V_{\mathcal{S}}} J_{\mathrm{s}}(\mathbf{r}_1, \mathbf{r}_2)\psi_{\mathbf{m}}(\mathbf{r}_2)\, \mathrm{d}^3\mathbf{r}_1 = \alpha_{\mathbf{m}}\psi_{\mathbf{m}}(\mathbf{r}_1). \tag{77}$$

The orthogonality of the eigenfunctions $\psi_{\mathbf{m}}$ is expressed by

$$\int_{V_{\mathcal{S}}} \psi_{\mathbf{m}}^*(\mathbf{r})\psi_{\mathbf{m}'}(\mathbf{r})\, \mathrm{d}^3\mathbf{r} = \delta_{\mathbf{m}\mathbf{m}'}. \tag{78}$$

It is straightforward to prove that the decomposition also holds in the spatial-spectral domain; i.e.,

$$\tilde{J}_{\mathrm{s}}(\mathbf{k}_1, \mathbf{k}_2) = \sum_{\mathbf{m}} \alpha_{\mathbf{m}} \tilde{\psi}_{\mathbf{m}}(\mathbf{k}_1)\tilde{\psi}_{\mathbf{m}}(\mathbf{k}_2). \tag{79}$$

Since the volume $V_{\mathcal{H}}$ occupied by the hologram is finite, we can decompose $\Delta\epsilon(\mathbf{r})$ into a Fourier series, according to

$$\Delta\tilde{\epsilon}(\mathbf{k}) = \sum_{\mathbf{j}} \epsilon_{\mathbf{j}} \tilde{\phi}_{\mathbf{j}}(\mathbf{k}), \quad \epsilon_{\mathbf{j}} = \int_{V_{\mathcal{H}}} \Delta\epsilon(\mathbf{r})\phi_{\mathbf{j}}(\mathbf{r})\, \mathrm{d}^3\mathbf{r}. \tag{80}$$

The orthogonality condition for the basis $\{\phi_{\mathbf{j}}\}_{\mathbf{j}\in\mathbb{N}^3}$ is expressed as

$$\int_{V_{\mathcal{H}}} \phi_{\mathbf{j}}^*(\mathbf{r})\phi_{\mathbf{j}'}(\mathbf{r})\, \mathrm{d}^2\mathbf{r} = \delta_{\mathbf{j}\mathbf{j}'}. \tag{81}$$

We seek to compute the coherent mode decomposition of the mutual intensity of the diffracted field in terms of the modes (76) of the source mutual intensity and the modes (80) of the volume hologram. In Appendix III we show that

$$\tilde{J}_{\mathrm{d}}(\mathbf{k}_1, \mathbf{k}_2) = \sum_{\mathbf{m}} \alpha_{\mathbf{m}} \tilde{\varphi}_{\mathbf{m}}^*(\mathbf{k}_1)\tilde{\varphi}_{\mathbf{m}}(\mathbf{k}_2) \tag{82}$$

where, for $|\mathbf{k}| = k$

$$\tilde{\varphi}_{\mathbf{m}}(\mathbf{k}) = \frac{1}{k_{\parallel}} \sum_{\mathbf{j}} \epsilon_{\mathbf{j}} \int_{\mathbb{R}^2} \tilde{\psi}_{\mathbf{m}}^*(\mathbf{k}')\tilde{\phi}_{\mathbf{j}}(\mathbf{k}' - \mathbf{k}) \frac{\mathrm{d}^2\mathbf{k}_{\perp}'}{k_{\parallel}'}. \tag{83}$$

In the space domain, the above expression can be rewritten as

$$\varphi_{\mathbf{m}}(\mathbf{r}) = \sum_{\mathbf{j}} \epsilon_{\mathbf{j}} \int_{V_{\mathcal{S}}} \int_{V_{\mathcal{H}}} \psi_{\mathbf{m}}^*(\mathbf{r}'')\phi_{\mathbf{j}}(\mathbf{r}') \cdot \frac{\exp\{ik(|\mathbf{r}'' - \mathbf{r}'| - |\mathbf{r}' - \mathbf{r}|)\}}{|\mathbf{r}'' - \mathbf{r}'|\, |\mathbf{r}' - \mathbf{r}|}\, \mathrm{d}^3\mathbf{r}'\, \mathrm{d}^3\mathbf{r}''. \tag{84}$$

Expressions (83) and (84) are the key results of this section: they express the modal structure of the diffracted field as a mixture of the coherence modes of the source and the modes of the volume hologram [note that the modes in (83) or (84) are not orthogonal but can be orthonormalized in straightforward fashion with a Gramm–Schmidt procedure]. The mixing occurs primarily through the coupling constants $\epsilon_{\mathbf{j}}$, i.e., the Fourier components of the refractive index modulation, while the modes $\tilde{\phi}_{\mathbf{j}}$ of the hologram itself act as weighting functions. Thus, the design problem is

defined in terms of (82) and (83) or (84): specify the Fourier components $\epsilon_{\mathbf{j}}$ such that the desired mutual coherence function $\tilde{J}_{\mathrm{d}}(\mathbf{k}_1, \mathbf{k}_2)$ is synthesized.

We will not attempt examples of modal design in this paper, but will point out two conclusions that follow from our results.

1) In the examples of Sections III-C and IV, the field is correlated with the particular spherical-reference mode of the volume hologram. This action is similar to a matched filter. The response, described by the degeneracy surfaces, is the set of object field modes that correlate with the hologram mode.
2) The response of the volume hologram can become much richer simply by following the modal synthesis approach delineated before; this is because the coupling coefficients $\epsilon_{\mathbf{j}}$ provide three degrees of design freedom ($\mathbf{j}$ is a three-element vector) thanks to the 3-D nature of the volume hologram.

VI. Conclusions and Discussion

In this paper we introduced the concept of using volume holograms for multidimensional imaging and demonstrated numerically various imaging functions that a volume hologram can perform. The specific geometries of confocal microscopy with volume holographic collector and color-selective tomography are of immediate interest, and we are currently working on experimental demonstrations. The modal approach outlined in Section V extends optical engineering design from the traditional surface-to-surface transformations to the most general domain of volume transformations. This "3-D optical engineering" approach is well tuned to the construction of hybrid optical systems, where optics perform analog transformations at the front end, while back-plane digital electronic computations provide the transformations that optical elements cannot do well (e.g., Fourier transforms on the intensity function, nonlinearities, etc.) thus completing the generality of the system. Including volume holograms as analog optical elements in the design permits maximum flexibility in the quest for the optimal system.

The commercial value of ubiquitous imaging will undoubtedly increase rapidly with the ongoing revolutions of digital and hybrid imaging. Humans are known to be "visual" animals, i.e., in most situations they respond optimally to visual stimulation. In many instances, sophisticated visual interfaces can drastically improve the performance of critical social functions as diverse as education of young children and national or corporate security. Advanced interfaces are also necessary in the domains of machine vision and machine learning for the improvement of algorithms or even the invention of new ones based on the availability of more complete visual information about the surrounding world. The endowment of optical systems with powerful elements, such as volume holograms, and new design approaches geared toward advanced imaging and visual interface is critical for the achievement of these technological advances in the near future.

Appendix I
Proof of the Correlation Property for the Diffraction of a Complex Field from a Volume Hologram

We will now prove assertion (73). Let us denote by

$$E_{\mathrm{i}}(\mathbf{r}) = \int_{V_{\mathcal{S}}} E_{\mathrm{s}}(\mathbf{r}'') \frac{\exp\{ikR''\}}{R''} \, \mathrm{d}^3\mathbf{r}'' \tag{85}$$

the field incident on location $\mathbf{r} \in V_{\mathcal{H}}$ of the volume hologram, where $R'' = |\mathbf{r} - \mathbf{r}''|$. Using Born's approximation, the field diffracted from the volume hologram is given by

$$E_{\mathrm{d}}(\mathbf{r}') = \int_{V_{\mathcal{H}}} E_{\mathrm{i}}(\mathbf{r}) \Delta\epsilon(\mathbf{r}) \frac{\exp\{ikR\}}{R} \, \mathrm{d}^3\mathbf{r} \tag{86}$$

$$= \int_{V_{\mathcal{S}}} \int_{V_{\mathcal{H}}} E_{\mathrm{s}}(\mathbf{r}'') \Delta\epsilon(\mathbf{r}) \frac{\exp\{ikR''\}}{R''} \frac{\exp\{ikR\}}{R} \cdot \mathrm{d}^3\mathbf{r} \, \mathrm{d}^3\mathbf{r}'' \tag{87}$$

where $R = |\mathbf{r}' - \mathbf{r}|$. We now use Weyl's identity for the expansion of a point source in a spectrum of plane waves

$$\frac{\exp\{ik|\mathbf{r}|\}}{|\mathbf{r}|} = \int_{\mathbb{R}^2} \frac{1}{k_{\|}} \exp\left\{ i\mathbf{k}_{\perp} \cdot \mathbf{r}_{\perp} + \sqrt{k^2 - |\mathbf{k}_{\perp}|^2} r_{\|} \right\} \mathrm{d}^2\mathbf{k}_{\perp}. \tag{88}$$

By using the notation

$$\boldsymbol{\kappa}(\mathbf{k}_{\perp}) = \mathbf{k}_{\perp} + \hat{\mathbf{n}} \sqrt{k^2 - |\mathbf{k}_{\perp}|^2}$$

for the "valid" wave vectors (i.e., the wave vectors that belong to the sphere $|\mathbf{k}| = k$, also known as the k-sphere), Weyl's identity is written in simpler form

$$\frac{\exp\{ik|\mathbf{r}|\}}{|\mathbf{r}|} = \int_{\mathbb{R}^2} \frac{1}{k_{\|}} \exp\{i\boldsymbol{\kappa}(\mathbf{k}_{\perp}) \cdot \mathbf{r}\} \, \mathrm{d}^2\mathbf{k}_{\perp}. \tag{89}$$

Substituting (89) into (87) we obtain successively

$$E_{\mathrm{d}}(\mathbf{r}') = \int_{V_{\mathcal{S}}} \int_{V_{\mathcal{H}}} \int_{\mathbb{R}^2} \int_{\mathbb{R}^2} E_{\mathrm{s}}(\mathbf{r}'') \Delta\epsilon(\mathbf{r}) \cdot \frac{\exp\{i\boldsymbol{\kappa}(\mathbf{k}_{1,\perp}) \cdot (\mathbf{r}' - \mathbf{r})\}}{k_{1,\|}} \cdot \frac{\exp\{i\boldsymbol{\kappa}(\mathbf{k}_{2,\perp}) \cdot (\mathbf{r} - \mathbf{r}'')\}}{k_{2,\|}} \, \mathrm{d}^2\mathbf{k}_{1,\perp} \, \mathrm{d}^2\mathbf{k}_{2,\perp} \, \mathrm{d}^3\mathbf{r} \, \mathrm{d}^3\mathbf{r}'' \tag{90}$$

$$= \int_{\mathbb{R}^2} \int_{\mathbb{R}^2} \cdot \left(\int_{V_{\mathcal{S}}} E_{\mathrm{s}}(\mathbf{r}'') \exp\{i\boldsymbol{\kappa}(\mathbf{k}_{2,\perp}) \cdot \mathbf{r}''\} \, \mathrm{d}^3\mathbf{r}'' \right) \cdot \left(\int_{V_{\mathcal{H}}} \Delta\epsilon(\mathbf{r}) \cdot \exp\{i(\boldsymbol{\kappa}(\mathbf{k}_{2,\perp}) - \boldsymbol{\kappa}(\mathbf{k}_{1,\perp})) \cdot \mathbf{r}\} \, \mathrm{d}^3\mathbf{r} \right) \cdot \exp\{i\boldsymbol{\kappa}(\mathbf{k}_{1,\perp}) \cdot \mathbf{r}'\} \frac{\mathrm{d}^2\mathbf{k}_{1,\perp} \, \mathrm{d}^2\mathbf{k}_{2,\perp}}{k_{1,\|} k_{2,\|}} \tag{91}$$

$$= \int_{\mathbb{R}^2} \int_{\mathbb{R}^2} \tilde{E}_{\rm s}(\boldsymbol{\kappa}(\mathbf{k}_{2,\perp}))\Delta\tilde{\epsilon}(\boldsymbol{\kappa}(\mathbf{k}_{2,\perp}) - \boldsymbol{\kappa}(\mathbf{k}_{1,\perp})) \cdot \exp\{i\boldsymbol{\kappa}(\mathbf{k}_{1,\perp}) \cdot \mathbf{r}'\} \frac{\mathrm{d}^2\mathbf{k}_{1,\perp}\, \mathrm{d}^2\mathbf{k}_{2,\perp}}{k_{1,\|}k_{2,\|}} \quad (92)$$

$$= \int_{\mathbb{R}^2} \left[\frac{\tilde{E}_{\rm s}}{k_\|} \star \Delta\tilde{\epsilon}^*\right]_{\boldsymbol{\kappa}(\mathbf{k}_{1,\perp})} \cdot \exp\{i\boldsymbol{\kappa}(\mathbf{k}_{1,\perp}) \cdot \mathbf{r}'\} \frac{\mathrm{d}^2\mathbf{k}_{1,\perp}}{k_{1,\|}}. \quad (93)$$

The last statement is equivalent to (73), which proves the assertion.

Appendix II
Proof of the Correlation Property for Statistical Fields

Assuming $E_{\rm s}$ is one realization of the random process representing the object, we form the correlations according to

$$J_{\rm s}(\mathbf{r}_1'', \mathbf{r}_2'') = \text{E.V.}\{E_{\rm s}(\mathbf{r}_1'')E_{\rm s}^*(\mathbf{r}_2'')\} \quad (94)$$

$$J_{\rm d}(\mathbf{r}_1', \mathbf{r}_2') = \text{E.V.}\{E_{\rm d}(\mathbf{r}_1')E_{\rm d}^*(\mathbf{r}_2')\}. \quad (95)$$

Substituting Born's diffraction formula (87) and (94) into (95), we obtain

$$J_{\rm d}(\mathbf{r}_1', \mathbf{r}_2') = \int_{V_{\mathcal{H}}} \int_{V_{\mathcal{H}}} \int_{V_{\mathcal{S}}} \int_{V_{\mathcal{S}}} \cdot J_{\rm s}(\mathbf{r}_1'', \mathbf{r}_2'')\Delta\epsilon(\mathbf{r}_1)\Delta\epsilon^*(\mathbf{r}_2) \times \frac{\exp\{ikR_1''\}}{R_1''} \frac{\exp\{ikR_2''\}}{R_2''} \frac{\exp\{ikR_1\}}{R_1} \cdot \frac{\exp\{ikR_2\}}{R_2}\, \mathrm{d}^3\mathbf{r}_1''\, \mathrm{d}^3\mathbf{r}_2''\, \mathrm{d}^3\mathbf{r}_1\, \mathrm{d}^3\mathbf{r}_2. \quad (96)$$

By using Weyl's identity and proceeding as in Appendix I, we obtain (75) after a long but straightforward calculation.

Appendix III
Derivation of the Coherent Mode Decomposition of the Field Diffracted by a Volume Hologram

To prove (82) we substitute (76) and (80) into (75). This leads to the expression

$$\tilde{J}_{\rm s}(\mathbf{k}_1, \mathbf{k}_2) = \sum_{\mathbf{m}} \sum_{\mathbf{j}_1} \sum_{\mathbf{j}_2} \alpha_{\mathbf{m}}\epsilon_{\mathbf{j}_1}^*\epsilon_{\mathbf{j}_2} \cdot \iint_{\mathbb{R}^2} \frac{\tilde{\psi}_{\mathbf{m}}^*(\boldsymbol{\kappa}_1'')\tilde{\psi}_{\mathbf{m}}(\boldsymbol{\kappa}_2'')}{k_{1,\|}k_{2,\|}k_{1,\|}''k_{2,\|}''} \tilde{\phi}_{\mathbf{j}_1}^* \cdot (\boldsymbol{\kappa}_1'' - \mathbf{k}_1)\tilde{\phi}_{\mathbf{j}_2}(\boldsymbol{\kappa}_2'' - \mathbf{k}_2)\, \mathrm{d}^2\mathbf{k}_{1,\perp}''\, \mathrm{d}^2\mathbf{k}_{2,\perp}''. \quad (97)$$

Rearranging the integrals and summations, we rewrite the above expression as

$$\tilde{J}_{\rm s}(\mathbf{k}_1, \mathbf{k}_2) = \sum_{\mathbf{m}} \alpha_{\mathbf{m}} \left(\sum_{\mathbf{j}_1} \epsilon_{\mathbf{j}_1} \int_{\mathbb{R}^2} \cdot \frac{\tilde{\psi}_{\mathbf{m}}(\boldsymbol{\kappa}_1'')\tilde{\phi}_{\mathbf{j}_1}(\boldsymbol{\kappa}_1'' - \mathbf{k}_1)}{k_{1,\|}k_{1,\|}''}\, \mathrm{d}^2\mathbf{k}_{1,\perp}''\right)^* \times \left(\sum_{\mathbf{j}_2} \epsilon_{\mathbf{j}_2} \int_{\mathbb{R}^2} \cdot \frac{\tilde{\psi}_{\mathbf{m}}(\boldsymbol{\kappa}_2'')\tilde{\phi}_{\mathbf{j}_2}(\boldsymbol{\kappa}_2'' - \mathbf{k}_2)}{k_{2,\|}k_{2,\|}''}\, \mathrm{d}^2\mathbf{k}_{2,\perp}''\right) \quad (98)$$

The last expression is equivalent to (82) by using definition (83) for the $\varphi_{\mathbf{m}}$'s. The alternative expression (84) follows from (83) by using Weyl's identity in reverse, in order to go back to the space domain.

Acknowledgment

The authors are grateful to Dr. F. T. S. Yu for the invitation to contribute this article, and to D. L. Marks for illuminating discussions on a number of related topics.

References

[1] P. J. van Heerden, "Theory of optical information storage in solids," *Appl. Opt.*, vol. 2, no. 4, pp. 393–400, 1963.

[2] A. Ashkin, G. D. Boyd, J. M. Dziedzic, R. G. Smith, A. A. Ballman, and K. Nassau, "Optically-induced refractive index inhomogeneities in $LiNbO_3$," *Appl. Phys. Lett.*, vol. 9, p. 72, 1966.

[3] F. S. Chen, J. T. LaMacchia, and D. B. Fraser, "Holographic storage in lithium niobate," *Appl. Phys. Lett.*, vol. 15, no. 7, pp. 223–225, 1968.

[4] D. Psaltis, "Parallel optical memories," *Byte*, vol. 17, no. 9, p. 179, 1992.

[5] J. F. Heanue, M. C. Bashaw, and L. Hesselink, "Volume holographic storage and retrieval of digital data," *Science*, vol. 265, no. 5173, pp. 749–752, 1994.

[6] D. Psaltis and F. Mok, "Holographic memories," *Sci. Amer.*, vol. 273, no. 5, pp. 70–76, 1995.

[7] Y. S. Abu-Mostafa and D. Psaltis, "Optical neural computers," *Sci. Amer.*, vol. 256, no. 3, pp. 66–73, 1987.

[8] J. Hong, "Applications of photorefractive crystals for optical neural networks," *Opt. Quant. Electr.*, vol. 25, no. 9, pp. S551–S568, 1993.

[9] D. J. Brady, A. G.-S. Chen, and G. Rodriguez, "Volume holographic pulse shaping," *Opt. Lett.*, vol. 17, no. 8, pp. 610–612, 1992.

[10] P.-C. Sun, Y. Fainman, Y. T. Mazurenko, and D. J. Brady, "Space-time processing with photorefractive volume holography," *Proc. SPIE*, vol. 2529, pp. 157–170, 1995.

[11] P.-C. Sun, Y. T. Mazurenko, W. S. C. Chang, P. K. L. Yu, and Y. Fainman, "All-optical parallel-to-serial conversion by holographic spatial-to-temporal frequency encoding," *Opt. Lett.*, vol. 20, no. 16, pp. 1728–1730, 1995.

[12] K. Purchase, D. Brady, G. Smith, S. Roh, M. Osowski, and J. J. Coleman, "Integrated optical pulse shapers for high-bandwidth packet encoding," *Proc. SPIE*, vol. 2613, pp. 43–51, 1996.

[13] D. M. Marom, P.-C. Sun, and Y. Fainman, "Analysis of spatial-temporal converters for all-optical communication links," *Appl. Opt.*, vol. 37, no. 14, pp. 2858–2868, 1998.

[14] G. A. Rakuljic and V. Levya, "Volume holographic narrowband optical filter," *Opt. Lett.*, vol. 18, no. 6, pp. 459–461, 1993.

[15] C. Mead, "Neuromorphic electronic systems," *Proc. IEEE*, vol. 78, pp. 1629–1636, Sept. 1990.
[16] ——, "Scaling of MOS technology to submicrometer feature sizes," *Analog Int. Circuits Signal Processing*, vol. 6, no. 1, pp. 9–25, 1994.
[17] G. Barbastathis, M. Levene, and D. Psaltis, "Shift multiplexing with spherical reference waves," *Appl. Opt.*, vol. 35, pp. 2403–2417, 1996.
[18] E. N. Leith, A. Kozma, J. Upatnieks, J. Marks, and N. Massey, "Holographic data storage in three-dimensional media," *Appl. Opt.*, vol. 5, no. 8, pp. 1303–1311, 1966.
[19] H. Kogelnik, "Coupled wave theory for thick hologram gratings," *Bell Syst. Tech. J.*, vol. 48, no. 9, pp. 2909–2947, 1969.
[20] D. L. Staebler, J. J. Amodei, and W. Philips, "Multiple storage of thick holograms in $LiNbO_3$," in *Proc. VII Int. Quantum Electronics Conf.*, Montreal, P.Q., Canada, 1972.
[21] D. A. Parthenopoulos and P. M. Rentzepis, "Two-photon volume information storage in doped polymer systems," *J. Appl. Phys.*, vol. 68, no. 11, pp. 5814–5818, 1990.
[22] F. H. Mok, M. C. Tackitt, and H. M. Stoll, "Storage of 500 high-resolution holograms in a $LiNbO_3$ crystal," *Opt. Lett.*, vol. 16, no. 8, pp. 605–607, 1991.
[23] F. H. Mok, "Angle-multiplexed storage of 5000 holograms in lithium niobate," *Opt. Lett.*, vol. 18, no. 11, pp. 915–917, 1991.
[24] F. H. Mok, G. W. Burr, and D. Psaltis, "Angle and space multiplexed random access memory (HRAM)," *Opt. Memory Neural Networks*, vol. 3, no. 2, pp. 119–127, 1994.
[25] R. A. Miller, G. W. Burr, Y.-C. Tai, D. Psaltis, C.-M. Ho, and R. R. Katti, "Electromagnetic MEMS scanning mirrors for holographic data storage," in *Proc. Solid-State Sensor and Actuator Workshop, Tranducer Research Foundation*, Cleveland Heights, OH, 1996, pp. 183–186.
[26] X. An and D. Psaltis, "Experimental characterization of an angle-multiplexed holographic memory," *Opt. Lett.*, vol. 20, no. 18, pp. 1913–1915, 1995.
[27] I. McMichael, W. Christian, D. Pletcher, T. Y. Chang, and J. Hong, "Compact holographic storage demonstrator with rapid access," *Appl. Opt.*, vol. 35, no. 14, pp. 2375–2379, 1996.
[28] D. P. Resler, D. S. Hobbs, R. C. Sharp, L. J. Friedman, and T. A. Dorschner, "High-efficiency liquid-crystal optical phased-array beam steering," *Opt. Lett.*, vol. 21, no. 9, pp. 689–691, 1996.
[29] J.-J. P. Drolet, E. Chuang, G. Barbastathis, and D. Psaltis, "Compact, integrated dynamic holographic memory with refreshed holograms," *Opt. Lett.*, vol. 22, no. 8, pp. 552–554, 1997.
[30] G. A. Rakuljic, V. Levya, and A. Yariv, "Optical data storage by using orthogonal wavelength-multiplexed volume holograms," *Opt. Lett.*, vol. 17, no. 20, pp. 1471–1473, 1992.
[31] S. Yin, H. Zhou, F. Zhao, M. Wen, Y. Zang, J. Zhang, and F. T. S. Yu, "Wavelength-multiplexed holographic storage in a sensitive photorefractive crystal using a visible-light tunable diode-laser," *Opt. Commun.*, vol. 101, nos. 5–6, pp. 317–321, 1993.
[32] C. Denz, G. Pauliat, and G. Roosen, "Volume hologram multiplexing using a deterministic phase encoding method," *Opt. Commun.*, vol. 85, pp. 171–176, 1991.
[33] D. Psaltis, M. Levene, A. Pu, G. Barbastathis, and K. Curtis, "Holographic storage using shift multiplexing," *Opt. Lett.*, vol. 20, no. 7, pp. 782–784, 1995.
[34] M. Mansuripur and G. T. Sincerbox, "Principles and techniques of optical data storage," *Proc. IEEE*, vol. 85, pp. 1780–1796, Nov. 1997.
[35] A. Pu and D. Psaltis, "Holographic 3D disks using shift multiplexing," in *Summaries of Papers Presented CLEO'96*, Baltimore, MD, p. 165.
[36] ——, "Holographic data storage with 100 bits/μm^2 density," in *Proc. Optical Data Storage Topical Meeting*, Tuscon, AZ, 1997, pp. 48–49.
[37] H. Lee, X.-G. Gu, and D. Psaltis, "Volume holographic interconnections with maximal capacity and minimal cross talk," *J. Appl. Phys.*, vol. 65, no. 6, pp. 2191–2194, 1989.
[38] K. Curtis, A. Pu, and D. Psaltis, "Method for holographic storage using peristrophic multiplexing," *Opt. Lett.*, vol. 19, no. 13, pp. 993–994, 1994.
[39] S. Campbell, X. M. Yi, and P. Yeh, "Hybrid sparse-wavelength angle multiplexed optical data storage system," *Opt. Lett.*, vol. 19, no. 24, pp. 2161–2163, 1994.
[40] G. T. Sincerbox, "Holographic storage—The quest for the ideal material continues," *Opt. Mat.*, vol. 4, nos. 2–3, pp. 370–375, 1995.
[41] M.-P. Bernal, G. W. Burr, H. Coufal, R. K. Grygier, J. A. Hoffnagle, C. M. Jefferson, R. M. McFarlane, R. M. Shelby, G. T. Sincerbox, and G. Wittmann, "Holographic-data-storage materials," *MRS Bull.*, vol. 21, no. 9, pp. 51–60, 1996.
[42] N. V. Kukhtarev, V. B. Markov, S. G. Odulov, M. S. Soskin, and V. L. Vinetskii, "Holographic storage in electrooptic crystals, I. Steady state," *Ferroelect.*, vol. 22, pp. 949–960, 1979.
[43] T. J. Hall, R. Jaura, L. M. Connors, and P. D. Foote, "The photorefractive effect—A review," *Progress Quantum Electron.*, vol. 10, no. 2, pp. 77–145, 1985.
[44] P. Yeh, *Introduction to Photorefractive Nonlinear Optics*. New York: Wiley, 1993.
[45] D. Psaltis, D. Brady, and K. Wagner, "Adaptive optical networks using photorefractive crystals," *Appl. Opt.*, vol. 27, no. 9, pp. 1752–1759, 1988.
[46] F. Mok, G. W. Burr, and D. Psaltis, "A system metric for holographic memory systems," *Opt. Lett.*, vol. 21, no. 12, pp. 896–898, 1996.
[47] G. Barbastathis, J.-J. P. Drolet, E. Chuang, and D. Psaltis, "Compact terabit random-access memory implemented with photorefractive crystals," in *Proc. SPIE Photorefractive Fiber and Crystal Devices: Materials, Optical Properties and Applications III*, San Diego, CA, 1997, pp. 107–122.
[48] N. V. Kukhtarev, V. B. Markov, S. G. Odulov, M. S. Soskin, and V. L. Vinetskii, "Holographic storage in electrooptic crystals, II. Beam coupling—Light amplification," *Ferroelect.*, vol. 22, pp. 961–964, 1979.
[49] P. Yeh, "Two-wave mixing in nonlinear media," *IEEE J. Quantum Electron.*, vol. 25, pp. 484–519, 1989.
[50] A. Yariv, "Phase-conjugate optics and real-time holography," *IEEE J. Quantum Electron*, vol. 14, pp. 650–660, 1978.
[51] J. Feinberg, "Self-pumped continuous-wave phase conjugator using internal reflection," *Opt. Lett.*, vol. 7, no. 10, pp. 486–488, 1982.
[52] D. Z. Anderson and J. Feinberg, "Optical novelty filters," *IEEE J. Quantum Electron*, vol. 25, pp. 635–647, Mar. 1989.
[53] M. Segev, B. Crosignani, and A. Yariv, "Spatial solitons in photorefractive media," *Phys. Rev. Let.*, vol. 68, no. 7, pp. 923–926, 1992.
[54] M.-F. Shih, Z. Chen, M. Mitchell, M. Segev, H. Lee, R. S. Feigelson, and J. P. Wilde, "Waveguides induced by photorefractive screening solitons," *J. Opt. Soc. Amer. B*, vol. 14, no. 11, pp. 3091–3101, 1997.
[55] J. J. Amodei and D. L. Staebler, "Holographic pattern fixing in electro-optic crystals," *Appl. Phys. Lett.*, vol. 18, no. 12, pp. 540–542, 1971.
[56] D. L. Staebler, W. J. Burke, W. Phillips, and J. J. Amodei, "Multiple storage and erasure of fixed holograms in Fe-doped $LiNbO_3$," *Appl. Phys. Lett.*, vol. 26, no. 4, pp. 182–184, 1975.
[57] G. Montemezzani and P. Gunter, "Thermal hologram fixing in pure and doped $KNbO_3$ crystals," *J. Opt. Soc. Amer. B*, vol. 7, no. 12, pp. 2323–2328, 1990.
[58] D. Zhang, Y. Zhang, C. Li, Y. Chen, and Y. Zhu, "Thermal fixing of holographic gratings in $BaTiO_3$," *Appl. Opt.*, vol. 34, no. 23, pp. 5241–5246, 1995.
[59] J. F. Heanue, M. C. Bashaw, A. J. Daiber, R. Snyder, and L. Hesselink, "Digital holographic storage system incorporating thermal fixing in lithium niobate," *Appl. Opt.*, vol. 21, no. 19, pp. 1615–1617, 1996.
[60] A. Y. Liu, M. C. Bashaw, L. Hesselink, M. Lee, and R. S. Feigelson, "Observation and thermal fixing of holographic gratings in lead barium niobate crystal," *Opt. Lett.*, vol. 22, no. 3, pp. 187–189, 1997.
[61] F. Micheron and G. Bismuth, "Electrical control of fixation and erasure of holographic patterns in ferroelectric materials," *Appl. Phys. Lett.*, vol. 20, no. 2, pp. 79–81, 1972.
[62] Y. Qiao, S. Orlov, D. Psaltis, and R. R. Neurgaonkar, "Electrical fixing of photorefractive holograms in $(Sr_{0.75}Ba_{0.25})Nb_2O_6$," *Opt. Lett.*, vol. 18, no. 12, pp. 1004–1006, 1993.
[63] M. Horowitz, A. Bekker, and B. Fischer, "Image and hologram fixing method with $(Sr_xBa_{1-x})Nb_2O_6$ crystals," *Opt. Lett.*, vol. 18, no. 22, pp. 1964–1966, 1993.
[64] R. S. Cudney, J. Fousek, M. Zgonik, P. Günter, M. H. Garrett, and D. Rytz, "Photorefractive and domain gratings in barium titanate," *Appl. Phys. Lett.*, vol. 63, no. 25, pp. 3399–3401, 1993.

[65] J. Ma, T. Chang, J. Hong, R. R. Neurgaonkar, G. Barbastathis, and D. Psaltis, "Electrical fixing of 1,000 angle-multiplexed holograms in SBN:75," *Opt. Lett.*, vol. 22, no. 14, pp. 1116–1118, 1997.
[66] H. C. Külich, "A new approach to read volume holograms at different wavelengths," *Opt. Commun.*, vol. 64, no. 5, pp. 407–411, 1987.
[67] ——, "Reconstructing volume holograms without image field losses," *Appl. Opt.*, vol. 30, no. 20, pp. 2850–2857, 1991.
[68] D. Psaltis, F. Mok, and H.Y.-S. Li, "Nonvolatile storage in photorefractive crystals," *Opt. Lett.*, vol. 19, no. 3, pp. 210–212, 1994.
[69] G. Barbastathis and D. Psaltis, "Shift-multiplexed holographic memory using the two-lambda method," *Opt. Lett.*, vol. 21, no. 6, pp. 429–431, 1996.
[70] E. Chuang and D. Psaltis, "Storage of 1,000 holograms with use of a dual-wavelength method," *Appl. Opt.*, vol. 36, no. 32, pp. 8445–8454, 1997.
[71] D. von der Linde, A. M. Glass, and K. F. Rodgers, "Multiphoton photorefractive processes for optical storage in $LiNbO_3$," *Appl. Phys. Lett.*, vol. 25, no. 3, pp. 155–157, 1974.
[72] ——, "Optical storage using refractive index change induced by two-step excitation," *J. Appl. Phys.*, vol. 47, no. 1, pp. 217–220, 1976.
[73] K. Buse, L. Holtmann, and E. Krätzig, "Activation of $BaTiO_3$ for infrared holographic recording," *Opt. Commun.*, vol. 85, no. 2, pp. 183–186, 1991.
[74] K. Büse, F. Jermann, and E. Krätzig, "Infrared holographic recording in $LiNbO_3$:Cu," *Appl. Phys. A*, vol. 58, no. 3, pp. 191–195, 1994.
[75] K. Büse, A. Adibi, and D. Psaltis, "Non-volatile holographic storage in doubly doped lithium niobate crystals," *Nature*, vol. 393, no. 6686, pp. 665–668, 1998.
[76] D. Psaltis, X. An, G. Barbastathis, A. Adibi, and E. Chuang, "Nonvolatile holographic storage in photorefractive materials," *SPIE Critical Rev.*, vol. CR65, pp. 181–213, 1997.
[77] K. Curtis and D. Psaltis, "Recording of multiple holograms in photopolymer films," *Appl. Opt.*, vol. 31, no. 35, pp. 7425–7428, 1992.
[78] U.-S. Rhee, H. J. Caulfield, and C. S. Vikram, and M. M. Mirsalehi, "Characteristics of the Du Pont photopolymer for angularly multiplexed page-oriented holographic memories," *Opt. Eng.*, vol. 32, no. 8, pp. 1839–1847, 1993.
[79] K. Curtis and D. Psaltis, "Characterization of the Du-Pont photopolymer for 3-dimensional holographic storage," *Appl. Opt.*, vol. 33, no. 23, pp. 5396–5399, 1994.
[80] A. Pu, K. Curtis, and D. Psaltis, "A new method for holographic data storage in photopolymer films," in *Proc. IEEE Nonlinear Optics: Materials, Fundamentals and Applications*, Waikoloa, HI, 1994.
[81] A. Pu and D. Psaltis, "High density recording in photopolymer-based holographic 3D disks," *Appl. Opt.*, vol. 35, no. 14, pp. 2389–2398, 1996.
[82] J. E. Ludman, J. Riccobono, J. Caulfield, J.-M. Fournier, I. Semenova, N. Rienhand, P. R. Hemmer, and S. M. Shahriar, "Porous-matrix holography for nonspatial filtering of lasers," *Proc. SPIE*, vol. 2406, pp. 76–85, 1995.
[83] J. E. Ludman, J. R. Riccobono, N. O. Rienhand, I. V. Semenova, Y. L. Korzinin, S. M. Shahriar, H. J. Caulfield, J.-M. Fournier, and P. Hemmer, "Very thick holographic nonspatial filtering of laser beams," *Opt. Eng.*, vol. 36, no. 6, pp. 76–85, 1997.
[84] G. J. Steckman, I. Solomatine, G. Zhou, and D. Psaltis, "Characterization of phenanthrenequinone-doped poly(methyl methacrylate) for holographic memory," *Opt. Lett.*, vol. 23, no. 16, pp. 1310–1312, 1998.
[85] H.-Y. S. Li, and D. Psaltis, "Three dimensional holographic disks," *Appl. Opt.*, vol. 33, no. 17, pp. 3764–3774, 1994.
[86] B. J. Goertzen and P. A. Mitkas, "Error-correcting code for volume holographic storage of a relational database," *Opt. Lett.*, vol. 20, no. 15, pp. 1655–1657, 1995.
[87] M. A. Neifeld and J. D. Hayes, "Error-correction schemes for volume optical memories," *Appl. Opt.*, vol. 34, no. 35, pp. 8183–8191, 1995.
[88] J. F. Heanue, k. Gurkan, and L. Hesselink, "Signal detection for page-access optical memories with intersymbol interference," *Appl. Opt.*, vol. 35, no. 14, pp. 2431–2438, 1996.
[89] G. W. Burr, J. Ashley, H. Coufal, R. K. Grygier, J. A. Hoffnagle, C. M. Jefferson, and B. Marcus, "Modulation coding for pixel-matched holographic data-storage," *Opt. Lett.*, vol. 20, no. 9, pp. 639–641, 1997.
[90] G. W. Burr, H. Coufal, R. K. Grygier, J. A. Hofnagle, and C. M. Jefferson, "Noise reduction of page-oriented data storage by inverse filtering during recording," *Opt. Lett.*, vol. 5, no. 15, pp. 289–291, 1998.
[91] R. M. Shelby, J. A. Hoffnagle, G. W. Burr, C. M. Jefferson, M.-P. Bernal, H. Coufal, R. K. Grygier, H. Gunther, R. M. McFarlane, and G. T. Sincerbox, "Pixel-matched holographic data storage with megabit pages," *Opt. Lett.*, vol. 22, no. 19, pp. 1509–1511, 1997.
[92] G. Barbastathis, "Intelligent holographic databases," Ph.D. dissertation, California Inst. Technol., Pasadena, 1998.
[93] J. W. Goodman, *Introduction to Fourier Optics*. New York: McGraw–Hill, 1968.
[94] C. Gu, J. Hong, and S. Campbell, "2-d shift-invariant volume holographic correlator," *Opt. Commun.*, vol. 88, nos. 4–6, pp. 309–314, 1992.
[95] F. T. S. Yu and S. Yin, "Bragg diffraction-limited photorefractive crystal-based correlators," *Opt. Eng.*, vol. 34, no. 8, pp. 2224–2231, 1995.
[96] J. R. Goff, "Experimental realization of a multiproduct photorefractive correlation system for temporal signals," *Appl. Opt.*, vol. 36, no. 26, pp. 6627–6635, 1997.
[97] F. T. S. Yu, "Optical neural networks: architecture, design and models," *Progr. Opt.*, vol. 32, pp. 61–144, 1993.
[98] H.-Y. S. Li, Y. Qiao, and D. Psaltis, "Optical network for real-time face recognition," *Appl. Opt.*, vol. 32, no. 26, pp. 5026–5035, 1993.
[99] A. Pu, R. Denkewalter, and D. Psaltis, "Real-time vehicle navigation using a holographic memory," *Opt. Eng.*, vol. 36, no. 10, pp. 2737–2746, 1997.
[100] M. Minsky, "Microscopy apparatus," U.S. Patent. 3 013 467, 1961.
[101] C. J. R. Sheppard and A. Choudhury, "Image formation in the scanning microscope," *Opt. Acta*, vol. 24, pp. 1051–1073, 1977.
[102] C. J. R. Sheppard and C. J. Cogswell, "Three-dimensional image formation in confocal microscopy," *J. Microscopy*, vol. 159, no. 2, pp. 179–194, 1990.
[103] C. J. Cogswell and C. J. R. Sheppard, "Confocal differential interference contrast (DIC) microscopy: Including a theoretical analysis of conventional and confocal DIC imaging," *J. Microscopy*, vol. 165, no. 1, pp. 81–101, 1992.
[104] I. J. Cox, C. J. R. Sheppard, and T. Wilson, "Super-resolution by confocal fluorescence microscopy," *Optik*, vol. 60, pp. 391–396, 1982.
[105] P. T. C. So, T. French, W. M. Yu, K. M. Berland, C. Y. Dong, and E. Gratton, "Time-resolved fluorescence microscopy using two-photon excitation," *Bioimaging*, vol. 3, no. 2, pp. 49–63, 1995.
[106] P. H. Van Cittert, *Physica*, vol. 1, p. 201, 1934.
[107] F. Zernike, *Proc. Phys. Soc.*, vol. 61, p. 158, 1948.
[108] V. Schooneveld, "Image formation from coherence functions in astronomy," in *Proc. IAU Colloquium*, vol. 49, Groningen, 1978.
[109] A. J. Devaney, "The inversion problem for random sources," *J. Math. Phys.*, vol. 20, pp. 1687–1691, 1979.
[110] W. H. Carter and E. Wolf, "Correlation theory of wavefields generated by fluctuating, three-dimensional, primary, scalar sources I. General theory," *Opt. Acta*, vol. 28, pp. 227–244, 1981.
[111] I. J. LaHaie, "Inverse source problem for three-dimensional partially coherent sources and fields," *J. Opt. Soc. Amer. A*, vol. 2, pp. 35–45, 1985.
[112] A. M. Zarubin, "Three-dimensional generalization of the van cittert-zernike theorem to wave and particle scattering," *Opt. Commun.*, vol. 100, nos. 5–6, pp. 491–507, 1992.
[113] J. Rosen and A. Yariv, "Three-dimensional imaging of random radiation sources," *Opt. Lett.*, vol. 21, no. 14, pp. 1011–1013, 1996.
[114] ——, "General theorem of spatial coherence: Application to three-dimensional imaging," *J. Opt. Soc. Amer. A*, vol. 13, no. 10, pp. 2091–2095, 1996.
[115] ——, "Reconstruction of longitudinal distributed incoherent sources," *Opt. Lett.*, vol. 21, no. 22, pp. 1803–1805, 1996.
[116] D. Marks, R. Stack, and D. J. Brady, "3D coherence imaging in the Fresnel domain," *Appl. Opt.*, vol. 38, no. 10, pp. 1332–1342, 1999.

[117] P. K. Rastogi, Ed., *Holographic Interferometry*. Berlin, Germany: Springer-Verlag, 1994.
[118] J. C. Wyant, "Two-wavelength interferometry," *Appl. Opt.*, vol. 10, p. 2113, 1971.
[119] C. Polhemus, "Two-wavelength interferometry," *Appl. Opt.*, vol. 12, no. 9, pp. 2071–2074, 1973.
[120] M. Bertero, P. Brianzi, and E. R. Pike, "Super-resolution in confocal scanning microscopy," *Inv. Probl.*, vol. 3, no. 2, pp. 195–212, 1987.
[121] M. Bertero, P. Boccacci, M. Defrise, C. De Mol, and E. R. Pike, "Super-resolution in confocal scanning microscopy. II. The incoherent case," *Inv. Probl.*, vol. 5, no. 4, pp. 441–461, 1989.
[122] M. Bertero, P. Boccacci, R. E. Davies, and E. R. Pike, "Super-resolution in confocal scanning microscopy. III. The case of circular pupils," *Inv. Probl.*, vol. 7, no. 5, pp. 655–674, 1991.
[123] M. Bertero, P. Boccacci, R. E. Davies, F. Malfanti, E. R. Pike, and J. G. Walker, "Super-resolution in confocal scanning microscopy. IV. Theory of data inversion by the use of optical masks," *Inv. Probl.*, vol. 8, no. 1, pp. 1–23, 1992.
[124] J. G. Walker, E. R. Pike, R. E. Davies, M. R. Young, G. J. Brakenhoff, and M. Bertero, "Superresolving scanning optical microscopy using holographic optical processing," *J. Opt. Soc. Amer. A*, vol. 10, no. 1, pp. 59–64, 1993.
[125] J. Grochmalicki, E. R. Pike, J. G. Walker, M. Bertero, P. Boccacci, and R. E. Davies, "Superresolving masks for incoherent scanning microscopy," *J. Opt. Soc. Amer. A*, vol. 10, no. 5, pp. 1074–1077, 1993.
[126] M. Bertero, P. Boccacci, F. Malfanti, and E. R. Pike, "Super-resolution in confocal scanning microscopy. V. Axial super-resolution in the incoherent case," *Inv. Probl.*, vol. 10, no. 5, pp. 1059–1077, 1994.
[127] D. Psaltis, D. Brady, X. G. Gu, and S. Lin, "Holography in artificial neural networks," *Nature*, vol. 343, no. 6256, pp. 325–330, 1990.
[128] D. Brady and D. Psaltis, "Control of volume holograms," *J. Opt. Soc. Amer. A*, vol. 9, no. 7, pp. 1167–1182, 1992.
[129] G. Barbastathis and D. Psaltis, "Multiplexing methods," in *Holographic Data Storage*, H. Coufal, L. Hesselink, and D. Psaltis, Eds. Berlin, Germany: Springer-Verlag, to be published.
[130] M. Born and E. Wolf, *Principles of Optics*, 6th ed. New York: Pergamon, 1980.
[131] J. W. Goodman, *Statistical Optics*. New York: Wiley, 1985.
[132] L. Mandel and E. Wolf, *Optical Coherence and Quantum Optics*. Cambridge, U.K.: Cambridge Univ. Press, 1995.

George Barbastathis (Member, IEEE) was born in Athens, Greece, in 1971. He received the Diploma in electrical and computer engineering from the National Technical University of Athens in 1993 and the M.Sc. and Ph.D. degrees in electrical engineering from the California Institute of Technology, Pasadena, in 1994 and 1997, respectively. His doctoral dissertation was entitled "Intelligent Holographic Databases."

After postdoctoral work at the University of Illinois, Urbana-Champaign, he joined the faculty at the Massachusetts Institute of Technology, Cambridge, in 1999 as Assistant Professor of Mechanical Engineering. He has extensive experience in the design of holographic memory architectures, interferometric sensors, and learning algorithms. His current research interests are in the applications of optical engineering to machine vision, visual learning, and human–computer interaction, and in optical product design.

Dr. Barbastathis is member of the Optical Society of America and the American Association for the Advancement of Science.

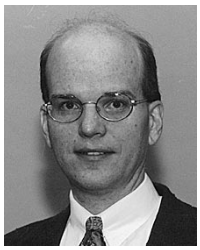

David J. Brady (Member, IEEE) received the B.A. degree in physics and math from Macalester College, St. Paul, MN, in 1985 and the M.S. and Ph.D. degrees in applied physics from the California Institute of Technology, Pasadena, in 1986 and 1990, respectively.

He is an Associate Professor of Electrical and Computer Engineering and a Research Associate Professor in the Beckman Institute for Advanced Science and Technology at the University of Illinois at Urbana-Champaign. His research focuses on optical systems for sensor and communications applications. His main research accomplishments include studies of the control and information capacity of volume holograms, a demonstration of ultrafast three-dimensional (3-D) space-time pulse shaping, and various demonstrations of interferometric and tomographic 3-D imaging.